

Regional flow conditions associated with stratocumulus cloud-clearing events over the southeast Atlantic

By

© 2019

Laura M. Tomkins

Submitted to the graduate degree program in Geography and Atmospheric Sciences and the Graduate Faculty of the University of Kansas in partial fulfillment of the requirements for the degree of Master of Sciences.

Chair: David B. Mechem

Sandra E. Yuter

David A. Rahn

Date Defended: 18 July 2019

The thesis committee for Laura M. Tomkins certifies that this is the approved version of the following thesis:

Regional flow conditions associated with stratocumulus cloud-clearing events over the southeast Atlantic

Chair: David B. Mechem

Date Approved: 24 July 2019

Abstract

Large, abrupt clearing events have been documented in the marine stratocumulus cloud deck that resides over the subtropical Southeast Atlantic Ocean. In these events, clouds are rapidly eroded along a line hundreds-to-thousands of kilometers in length that generally moves westward away from the African coast. Because marine stratocumulus clouds exert a strong cooling effect on the planet, any phenomenon that acts to erode large areas of low clouds may be climatically important. Previous satellite-based research has suggested that the cloud-clearing events may be caused by westward-propagating atmospheric gravity waves rather than simple advection of the cloud boundary. The gravity waves are hypothesized to be excited by an interaction between offshore flow from the African continent and the stratocumulus-topped marine boundary layer. The Weather Research and Forecasting (WRF) model is used to explore the nature of the offshore flow, which is a fundamental physical mechanism behind the dramatic clearing events. Results are presented from two series of week-long simulations driven by ERA-Interim reanalysis in the month of May when cloud-clearing boundaries exhibit maximum frequency. One series covers a period containing multiple cloud-clearing episodes (active period), and the second series covers a period without any cloud-clearing episodes (null period). Synoptic analysis, Hovmöller diagrams, and passive tracers are used to assess the character of the diurnal west-African coastal circulation. Our results indicate that the active period regularly experiences offshore flow from the continent above the boundary layer overnight, whereas the null period is associated with predominantly onshore flow along the coast particularly in the afternoon. The offshore flow overrunning the boundary layer can extend hundreds of kilometers westward of the coast. We document 900-hPa disturbances in each period, which influence the coastal flow of the region. Additionally, we find that the boundary layer height is higher in the

null period than in the active period, suggesting that the active periods are associated with areas of thinner clouds that may be more susceptible to cloud-clearing events.

Acknowledgments

I would first like to give a big thank you to my advisor, Dr. David Mechem, for all of his effort and support throughout this project. I would also like to thank my committee members, Dr. Sandra Yuter, for her feedback and guidance on this project, and Dr. David Rahn, for his time and valuable insight. Thank you to Luke McMichael for providing constructive discussion and helpful comments from the very beginning of this project. Thank you also to Spencer Rhodes for his input and analysis during this project. Thank you to all the Department of Geography and Atmospheric Science faculty and students for creating an encouraging, engaging, and enjoyable working environment. Last, I would like to thank my friends and family for all their continued support and motivation. This work was funded by the National Science Foundation grant number AGS-1656237.

Table of Contents

List of Tables	vii
List of Figures	viii
CHAPTER 1 Introduction.....	1
CHAPTER 2 Methods	9
2.1 Model Description	9
2.2 Project Design and Case Selection	11
2.3 Reanalysis Temperature Comparison	12
CHAPTER 3 Results	16
3.1 Synoptic Overview.....	16
3.2 Offshore Flow	19
3.2.1 900-hPa flow	19
3.2.2 900-hPa Geostrophic flow	21
3.2.2 Surface flow	23
3.2.3 Cross sections.....	24
3.2.4 Tracer fields	25
3.3 Boundary layer Height.....	27
CHAPTER 4 Discussion.....	43
4.1 Association of offshore flow with clearing periods.....	43
4.2 Near-coastal low-pressure features	44
4.3 Impacts of Boundary layer Height.....	45
CHAPTER 5 Summary and Conclusions	47
APPENDICES	50
Appendix A.....	50
Appendix B.....	52
Appendix C	53
Appendix D.....	55
REFERENCES	57

List of Tables

Table 2.1. Dates and clearing event characteristic (“yes”, “no”, “maybe”; see text for full description) of each simulation. Greyed shading indicates dates not analyzed to account for spin-up.....	12
Table A1. Average minimum temperature for different Boundary layer schemes.....	50

List of Figures

Figure 1.1. Cartoon graphic of sea breeze (left) and land breeze (right). Graphic from NC Climate Office, adapted from NOAA graphic https://climate.ncsu.edu/edu/Breezes	8
Figure 2.1. Precipitation from GPM for May 2015-2018 [mm/months]	13
Figure 2.2. WRF domain configuration for the simulations with terrain (m; contoured every 50 m). Mesh D01 (black box) has horizontal grid spacing of 10 km. Fine mesh simulations with grid spacing 3.33 km have been performed but are not included in this report or on this figure.	13
Figure 2.3. Vertical grid spacing in the model as a function of height for (a) lower 5 km and (b) full model vertical extent.	14
Figure 2.4. Diurnal cycle for (a) WRF, (b) ERA–Interim, (c) ERA5, and (d) MERRA2 data valid for 20 May 2013 0000 UTC to 27 May 2013 0000 UTC. 2-m temperatures (blue solid line) and skin temperatures (blue dashed line) are averaged over 15-20°S, 15-20°E.....	15
Figure 3.1. Simulated synoptic fields for two times during the active period (21 May 2013 0000 UTC [left column] and 24 May 2013 0000 UTC [right column]). (a) and (b) 500-hPa heights (m; contoured every 10 m) and wind (key in upper right). (c) and (d) 700-hPa heights and wind. (e) and (f) 900-hPa heights and wind. (g) and (h) SLP (hPa; contoured every 1 hPa) and 10 m winds. Black dashed line in panel (a) indicates the location of trough discussed in text.....	29
Figure 3.2. As in Fig. 3.1 but for two times during the null period. 22 May 2008 0000 UTC (left column) and 1600 UTC (right column). The red box in panel (f) indicates the area where Hovmöller diagrams are averaged over. The blue line in panel (f) indicates the location of cross sections.....	30
Figure 3.3. Hovmöller diagrams of 900-hPa (a) u (m s^{-1} ; contoured every 1 m s^{-1}), (b) v (m s^{-1} ; contoured every 1 m s^{-1}), and (c) w (cm s^{-1} ; contoured every 0.25 cm s^{-1}) during the active period. Hovmöller diagrams are calculated over the latitude range of 15°S to 20°S (red box in Fig. 3.2a). The black line in the bottom corner indicates the average coastline over this region and the bold grey line shows where the average coastline begins. Tick marks on y axis indicate time at 00 UTC.....	31
Figure 3.4. As in Fig. 3.3 but for the null period.	31
Figure 3.5. Hovmöller diagrams of the geostrophic and ageostrophic components of the 900-hPa wind components for the active period. (a) u_g , (b) u_a , (c) v_g , (d) v_a (m s^{-1} ; contoured every 1 m s^{-1}). As in Figs. 3.3 and 3.4, Hovmöller diagrams are calculated over the latitude range of 15°S to 20°S (red box in Fig. 3.2a). The black line in the bottom corner indicates the average coastline over this region and the bold grey line shows where the average coastline begins. Tick marks on y axis indicate time at 00 UTC.	32
Figure 3.6. As in Fig. 3.5 but for the null period.	32
Figure 3.7. ERA–Interim Hovmöller diagrams of the geostrophic and ageostrophic components of the 900-hPa u wind components for the active period; (a) u , (b) u_g , and (c) u_a (m s^{-1} ; contoured every 1 m s^{-1}). Hovmöller diagrams are calculated over the latitude range of 15°S to 20°S (red box in Fig. 3.2a). The bold grey line indicates where the average coastline begins. Tick marks on y axis indicate time at 00 UTC.	33
Figure 3.8. As in Fig. 3.7 but for null period.	33
Figure 3.9. Hovmöller diagrams of (a) 10-m u (m s^{-1} ; contoured every 1 m s^{-1}), (b) 10-m v (m s^{-1} ; contoured every 1 m s^{-1}), (c) SLP (hPa; contoured every 0.5 hPa), calculated over the latitude	

range of 15°S to 20°S (red box in Fig. 3.2a). The black line in the bottom corner indicates the average coastline over this region and the bold grey line shows where the average coastline begins. Tick marks on y axis indicate time at 00 UTC.....	34
Figure 3.10. As in Fig. 3.9 but for the null period.	34
Figure 3.11. Cross section along 15°S (blue line in Fig. 3.2a) of (a)–(d) w (shaded; contoured every 1 cm s ⁻¹ ; red indicates areas of upward motion, blue indicates areas of downward motion), u (grey lines; contoured every 1 m s ⁻¹ , dashed indicates negative (easterly) values) and boundary layer height (BLH, bold black line), (e)–(h) Temperature (shaded; contoured every 1 K) and BLH (bold black line), (i)–(l) u (shaded; contoured every 1 m s ⁻¹ ; orange indicates positive (westerly) motion, purple indicates negative (easterly) motion) and BLH (bold black line), valid every 4 hours from 22 May 2013 1400 UTC to 23 May 2013 0200 UTC from the active period.	35
Figure 3.12. As in Fig. 3.11 but for the null period, valid every 4 hours from 23 May 2008 1400 UTC to 24 May 2013 0200 UTC.	36
Figure 3.13. (a)–(b) Plan views of the simulated column-integrated ‘land’ passive tracer field (red shaded, dimensionless) for two times during the active period (21 May 2013 0000 UTC and 27 May 2013 0000 UTC). (c)–(d) Vertical cross section of tracer along 15.5°S line indicated in (a) and (b) and BLH (dashed black line).	37
Figure 3.14. As in Fig. 3.13 but for two times during the null period (22 May 2008 0000 UTC and 28 May 2008 0000 UTC).	38
Figure 3.15. Plan views of the simulated column-integrated ‘ocean’ passive tracer field (blue shaded, dimensionless) for the same two active period times as in Fig. 3.13. (c)–(d) Vertical cross section of tracer along 15.5°S line indicated in (a) and (b) and BLH (dashed black line)..	39
Figure 3.16. As in Fig. 3.13 but for the same two null period times as in Fig. 3.14.....	40
Figure 3.17. Calculated BLH (m; contoured every 100 m) for (a) active period valid 24 May 2013 0000 UTC and (b) null period valid 25 May 2008 0000 UTC.	41
Figure 3.18. Hovmöller diagrams of BLH (m; contoured every 25 m) for the for (a) active and (b) null periods. Hovmöller diagrams are calculated over the latitude range of 15°S to 20°S (red box in Fig. 3.2a). Tick marks on y axis indicate time at 00 UTC.....	41
Figure 3.19. Calculated median BLH (m) as a function of longitude calculated over a latitude range from 15°S to 20°S for the null period (green) and active period (blue) during the night (0200–0600 UTC; darker colors) and during the day (1400–1800 UTC; lighter colors). Shaded regions show the interquartile range.	42
Figure A1. Map of Africa showing temperature analysis region in black box.....	51
Figure A2. Diurnal cycle of temperature for (a) MYJ, (b) MYNN, and (c) Yonsei simulations. Temperatures averaged over box in Fig. A1.....	51
Figure C1. Map of Africa showing temperature analysis region in the black box.	53
Figure C2. Diurnal cycle for active period (blue, dashed line) and null period (green, solid line) for the region in Figure C1.....	54
Figure D1. Hovmöller diagrams of the geostrophic and ageostrophic components of the 950-hPa and 800-hPa horizontal wind for the active period. (a) 950-hPa u_g , (b) 950-hPa u_a , (c) 800-hPa u_g , and (d) 800-hPa u_a (m s ⁻¹ ; contoured every 1 m s ⁻¹). As in Figs. 3.3 and 3.4, Hovmöller diagrams are calculated over the latitude range of 15°S to 20°S (red box in Fig. 3.2a). The black	

line in the bottom corner indicates the average coastline over this region and the bold grey line shows where the average coastline begins. Tick marks on y axis indicate time at 00 UTC..... 55
Figure D2. As in Fig. D1 but for null period. 56

CHAPTER 1 Introduction

Stratocumulus clouds are an important component of the climate system. Stratocumulus cover vast areas of the planet and are more abundant than any other type of cloud (Wood 2012). In addition to their large areal coverage, they scatter back to space a large portion of incoming solar radiation, and because the cloud-top temperature is only slightly cooler than the underlying surface, they emit nearly the same amount of infrared radiation as the surface, thus exerting a strong cooling effect on the planet (Hartmann et al. 1992). Any large changes to stratocumulus area coverage or optical properties will therefore substantially impact the radiation budget. Unfortunately, representing stratocumulus in global climate models (GCMs) remains an ongoing challenge (Bony and Dufresne 2005; Wyant et al. 2015).

Stratocumulus cloud formation and maintenance is favored in regions of large-scale subsidence associated with the descending branch of the Hadley cell (Klein and Hartmann 1993). These conditions are typically observed over eastern subtropical oceans and are associated with a semi-permanent high-pressure system and associated anticyclonic flow. In contrast to the cool oceans, the neighboring continents are warmer and usually experience lower sea-level pressure. The resulting baroclinity near the coast, in combination with the Coriolis force, promotes a strong, equatorward, low-level jet along the coast between the subtropical high-pressure center and the continent (Garreaud and Muñoz 2005; Parish 2000). The coastal jet creates stress on the ocean surface, which via Ekman transport leads to the upwelling of cool, nutrient-rich water (Rutllant and Montecino 2002). The cool oceans also promote a stable environment in which subsidence maintains a strong temperature inversion. Stratocumulus clouds form below the temperature inversion at the top of the cool, moist marine boundary layer.

Recently, dramatic cloud-clearing boundaries have been observed in marine stratocumulus clouds over the southeast Atlantic (SEA) ocean off the western coast of Africa (Yuter et al. 2018). These clearing events exist as large regions (>1000 km) of sharp cloudiness transitions which cross the coast around local midnight and usually propagate westward at a speed of ~ 10 m s⁻¹. The stratocumulus cloud field rapidly erodes along these sharp boundaries, leaving behind either clear skies or significantly thinner clouds which allows increased solar radiation to reach the surface. Since the cloud clearing happens overnight, no shortwave feedbacks are required. Below the boundary layer, southerly flow is generally observed over this region during these events, associated with the climatologically dominant subtropical high pressure discussed above. Animations of the boundaries from satellite show the cloud field being advected northward and the boundary simultaneously moving westward, which indicates that this cloud-clearing phenomenon is not driven by the flow within the boundary layer and at cloud level.

Yuter et al. (2018) hypothesize that, instead of advection, gravity waves are the primary mechanism for eroding the cloud. The gravity waves are thought to be excited by an interaction between the offshore flow from the high terrain and the stratocumulus-topped boundary layer. A hypothetical gravity wave moving through the cloud field would influence cloud properties as follows. For a well-mixed boundary layer, upward wave motion increases the boundary layer depth, thickening the cloud by a proportional amount and increasing the liquid water path (LWP; note that LWP scales as the square of the cloud depth, i.e., $LWP \sim h^2$). Downward motion, on the other hand, reduces the boundary layer depth, resulting in a thinner cloud. Ordinarily, after the wave passes through, the cloud will return to its initial state. In the cloud-clearing cases, however, the cloud is usually almost or completely cleared. This cloud-clearing phenomenon, therefore, necessitates an irreversible aspect to the gravity-wave mechanism. In the gravity-wave

hypothesis, enhanced entrainment is proposed as the particular irreversibility mechanism, with stronger entrainment accompanying gravity-wave passage. Satellite observations of the cloud boundaries often show high-frequency wave features at the edge of the cloud boundaries, also suggesting that gravity waves may be a factor in the cloud-clearing events. Although the cloud field may not completely clear, owing to the dramatic nature of the clearing, we refer to these transformations as irreversible since over a short period the cloud remains eroded. After clearing, cloud usually reforms after several hours or at most a day later.

Cloud-eroding gravity waves in stratocumulus clouds have been documented in other work. In a regional modeling study, Garreaud and Muñoz (2004) documented a diurnal “upsidence” wave in stratocumulus clouds found over the southeast Pacific (SEP) ocean. A large area of upward motion, excited by diurnal heating of the elevated terrain of the Andes Mountains, propagates southwestward away from the land through the stratocumulus clouds. The upsidence area of the wave deepens the boundary layer, increases the turbulence and entrainment, and thus makes the boundary layer warmer and drier and erodes the cloud. Likewise, Rahn and Garreaud (2010) found evidence of the upsidence wave in their simulations of the boundary layer in the SEP. Upsidence waves have also been observed from satellite data (O'Dell et al. 2008). This SEP cloud-eroding phenomenon differs from the SEA cloud-clearing events because the upsidence wave feature tends to create a smaller area of cloud erosion, and the effects are not irreversible since the cloud reforms within a few hours after the wave passes through the area. The timing of these features also appears to occur earlier in the evening with the upsidence wave leaving the coast around 0000 UTC (1900 LST).

The mechanism leading to irreversible changes in the cloud field is not clear. Allen et al. (2013) documented areas of pockets of open cells (POCs; Stevens et al. 2005) in stratocumulus

clouds propagating against the mean flow. Allen et al. hypothesized that the propagating POCs were due to gravity waves associated with a disturbed subtropical jet stream. The upward motion of the wave moving through the cloud would thicken areas of the cloud, which would cause the cloud to precipitate and scavenge liquid water (Allen et al. 2013). Upon the passing of the full wave (both upward- and downward-moving phases), the resulting cloud would be thinner than the initial cloud, leading to the formation of POCs (Allen et al. 2013). Connolly et al. (2013) expanded on the work of Allen et al. with a modeling study to better understand the mechanisms governing cloud thinning. Connolly et al. concluded that in addition to the enhanced precipitation accompanying thickening of the cloud as the initial part of the wave passed, the LWP was also reduced by the entrainment of dry air and increased shortwave heating in the boundary layer. This work also differs from the cloud-clearing events in the SEA because, similar to Garreaud and Muñoz (2004), these events also appear to be reversible in that the cloud reforms a few hours after and they do not have the same sharp boundaries as in the SEA events.

Other wave features have been documented in coastal clouds near Australia. One phenomenon, the “Morning Glory,” is found over the Gulf of Carpentaria and features long bands of clouds (Clarke 1972). The bands of clouds are formed by the interaction of sea breezes on either side of the gulf. This interaction creates gravity waves over the region, which cause the formation of the clouds in the upward motion of the wave. Similarly, off the northwest coast of Australia, an interaction between the onshore sea breeze and offshore wind triggers waves, which create banded clouds similar to the Morning Glory events (Birch and Reeder 2013). However, these banded clouds and the Morning Glory are a phenomenon of cloud creation, not erosion.

Burleyson and Yuter (2015) examined diurnal cycles of cloud fraction over the SEA, SEP, and northeast Pacific (NEP). They found that the SEA region had the most substantial interseasonal variability of the three regions, which originally motivated the research into the cloud-clearing events. Stratocumulus over the SEA are observed to be thinner than stratocumulus clouds over the SEP (Zuidema et al. 2016). This difference suggests the possibility that the clouds in the SEA could be more susceptible to irreversible erosion mechanisms, relative to clouds in the SEP. However, the results of Zuidema et al. (2016) are ambiguous because their LWP statistics are not conditioned upon cloud and therefore are heavily influenced by cloud area fraction.

Coastal circulations are an important feature over this region and potentially have implications for the cloud-eroding boundaries. Figure 1.1 shows an idealized schematic of sea and land breezes. During the day, the land heats up more than the ocean which creates a localized low pressure over the land surface and strengthens the pressure gradient between the land and the ocean. This strengthened pressure gradient causes air to move from the ocean to the land and establishes offshore flow, known as a sea breeze. The opposite is true overnight when the land cools down and the pressure increases at the surface causing the air to move from the land to the ocean creating onshore flow, known as a land breeze. Additionally, the overnight land breeze will likely have some downslope component due to the highlands along the coast of Africa which also likely plays an important role in the cloud-eroding boundaries. The western coast of Africa is not straight but has a prominent bulge around 15°S which affects the flow patterns along the coast and is important for the coastal dynamics in this region.

Kloesel (1992) documented instances of stratocumulus cloud-clearing in the NEP off the coast of California during the First ISCCP (International Satellite Cloud Climatology Project)

Regional Experiment (FIRE) field campaign. The clouds clearings documented in Kloesel (1992) are large areas of clear skies which develop off the coast of California in regions where stratocumulus clouds typically exist. The clearings are observed for days at a time and have a diurnal cycle of expansion during the day and contraction overnight. These cloud clearings are associated with ridging of the subtropical anticyclone, which promotes offshore flow. Kloesel also noted that the subsidence associated with the high pressure may also influence these cloud-clearing events and potentially inhibits the clouds from redeveloping. Crosbie et al. (2016) expanded on this work by examining thermodynamic and aerosol properties across the clearing boundaries with aircraft measurements. In agreement with Kloesel, Crosbie et al. concluded that synoptic-scale perturbations are associated with the cloud-clearing events.

Rare occasions of stratocumulus cloud clearings in the SEP have been associated with high wind events (Garreaud and Rutllant 2003; Garreaud et al. 2002; George and Wood 2010; Rutllant and Garreaud 2004). The high wind events are driven by changes in the large scale synoptic patterns and so-called coastal lows at the surface (Rahn and Garreaud 2014). Garreaud et al. (2002) examined the typical conditions associated with these coastal lows. The lows form as troughs along the coast with high pressure over the ocean and land, referred to as a “High-Low-High” pattern. The coastal lows form with the passage of an upper-level ridge. Rutllant and Garreaud (2004) expanded on this work by exploring the flow patterns associated with these events using data from surface stations. They documented events of strong offshore and downslope flow in central Chile, known as “Raco” events, associated with the coastal lows. Their numerical simulations corroborated these findings and characterize the effects of the flow (Garreaud and Rutllant 2003). The flow coming off the continent is much drier and warmer than the air over the ocean so the flow can warm the boundary layer and erode the stratocumulus

clouds which exist over this region. Montecinos et al. (2017) employed similar approaches to investigate the “Puelche” winds in south-central Chile.

Previous investigations of clearing events in stratocumulus clouds largely differ from the observed cloud-clearing boundaries in the SEA. The cloud-clearing events over the SEA are unique in the fact that they have sharp boundaries and that the cloud remains eroded for up to a day, unlike the cloud-clearing phenomenon documented in stratocumulus clouds in the SEP. Additionally, the transient cloud-clearing events described in Yuter et al. (2018) differ from the longer clear periods described by Klosel (1992) and Crosbie et al. (2016), which are more directly influenced by the synoptic-scale conditions. That said, given the variability in SEA cloud-clearing events, it is likely that varying synoptic conditions likely play a role in promoting or suppressing them. These SEA cloud-clearing features are likely important from a climatological perspective, but they have not been studied to the extent of stratocumulus cloud clearings over other ocean basins. This project seeks to understand the physical processes associated with these events, specifically the diurnal and large-scale flow patterns, which impact the coastal mesoscale dynamics over this region. To this end, we simulate several periods in the SEA region with the Weather Research and Forecasting (WRF) model. The simulation methodology and experimental design are described in Chapter 2. Chapter 3 discusses the results of the simulations. Chapter 4 will consider the implications of the results, and Chapter 5 will present the conclusions of the study.

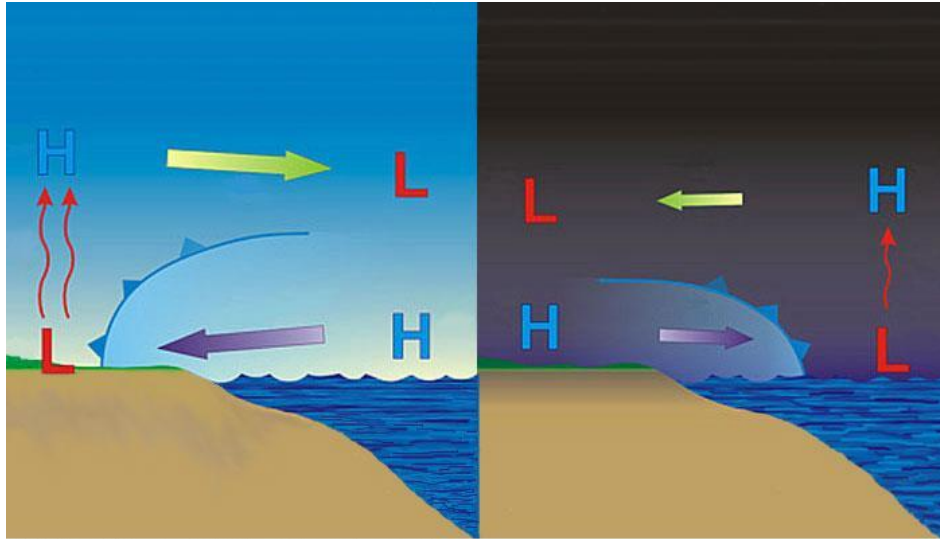


Figure 1.1. Cartoon graphic of sea breeze (left) and land breeze (right). Graphic from NC Climate Office, adapted from NOAA graphic <https://climate.ncsu.edu/edu/Breezes>

CHAPTER 2 Methods

The proposed cloud-clearing hypothesis from Yuter et al. (2018) is a multi-step process, which requires three separate mechanisms: offshore flow, excitation of gravity waves, and a quasi-irreversible clearing mechanism. This research focuses on examining and characterizing the first mechanism, the offshore flow.

2.1 Model Description

All simulations use the Advanced Research WRF (ARW) model (version 3.9.1), which is based on three-dimensional, nonhydrostatic, compressible dynamics (Skamarock et al. 2008). The Mellor–Yamada–Janjic (MYJ) boundary layer parameterization is employed to represent subgrid-scale vertical transports (Janjic 1994). Horizontal diffusion is parameterized using Smagorinsky first-order closure (Smagorinsky 1963). Microphysical processes are parameterized using the Morrison 2-moment scheme (Morrison et al. 2009). The Kain–Fritsch (KF) scheme is used for the cumulus parameterization (Kain 2004). It should be noted that deep convection is scarce over our domain (both over the land and the ocean), except for that associated with the Inter–Tropical Convergence Zone (ITCZ) or potentially any convection which develops over land (Fig. 2.1). All simulations employ the NOAH land surface model (Tewari et al. 2004). Longwave radiation is parameterized with the Rapid Radiative Transfer Model (RRTM) scheme, and the shortwave radiation is parameterized with the Dudhia scheme (Dudhia 1989; Mlawer et al. 1997). We ran a number of additional simulations with different boundary layer and cumulus parameterizations to test the sensitivity of the model to parameterization choice. Simulation results were not particularly sensitive to the choice of boundary layer and/or convective parameterizations. Analysis of these sensitivity simulations is discussed in Appendix A.

The domain for the simulations extends from $\sim 12^\circ\text{W}$ to $\sim 25^\circ\text{E}$ in the east-west direction and $\sim 0^\circ\text{N}$ to $\sim 28^\circ\text{S}$ in the north-south direction (Fig. 2.2). Horizontal grid spacing is 10 km with 430 points in the east-west direction and 298 in the north-south direction (4300 km x 2980 km), with a time step of 40 seconds (Fig. 2.2). The domain is configured to include a substantial portion of the continent, especially the plateau region, to better resolve the diurnal heating and cooling processes responsible for the land/sea breeze circulation. Because the cloud-clearing boundaries often move as far west as 4°W , the domain also extends well out over the ocean. Initial simulations included a fine (3.33 km), nested domain within the coarse domain. However, the coarse mesh was sufficient in capturing the salient mesoscale features of the coastal circulation. We suspect that examining the clouds and entrainment behavior in detail (which we do not do in this project) will require simulations with a finer mesh. The vertical grid has 82 points with variable grid spacing to adequately resolve the boundary layer and inversion structure. In the lower 5 km, the grid spacing ranges from 20 m to 400 m, and above that increases up to a maximum of 1000 m (Fig. 2.3). The grid spacing near the inversion height is ~ 100 m similar to the regional modeling study of Nelson et al. (2016).

European Centre for Medium-Range Forecasts (ECMWF) interim reanalysis (ERA–Interim; Dee et al. 2011) data, available every 6 hours (four times daily) with a 0.75° latitude/longitude grid spacing, provides initial and boundary conditions for the WRF simulations. Data assimilation update cycles are not employed throughout the simulation, so the ERA–Interim reanalysis influences the WRF simulations only via the boundary forcing. Sea Surface Temperature (SST) data is provided from ERA–Interim reanalysis. Following Nelson et al. (2016), we consider the first 24 h to be the spin-up period. Due to the coarse resolution of the ERA–Interim data, the initial conditions are very smooth. Over the first day, smaller-scale

disturbances consistent with the WRF grid resolution develop, and by ~24 hours the finer-scale variability in WRF has had a full chance to develop. We consider the model spin-up period to be complete when, visually, fine-scale structures have sufficiently developed.

2.2 Project Design and Case Selection

Instead of concentrating on specific clearing events, we performed a series of 7-day simulation periods. All simulation periods take place during May coinciding with the highest frequency of clearing events (Yuter et al. 2018). Future work will simulate events in other months. Of the four, 7-day simulations, two were “active” periods during which most of the days included cloud-clearing events, and two were “null” periods without clearing events. The active and null periods are so named because it is more likely to have a clearing event in May than not. The periods were classified as active or null based on Yuter et al. (2018), who characterized 1911 days over five years as either having cloud eroding boundaries present (“yes”), not having boundaries present (“no”), or possibly having boundaries present (“maybe”). Events were characterized using Moderate Resolution Imaging Spectroradiometer (MODIS) corrected reflectance data from the Aqua and Terra satellites (see methods of Yuter et al. (2018) for full details). We chose two periods of both active and null simulations to provide context and increase confidence in the results of each simulation. Table 2.1 shows the dates spanned by each simulation and whether each day had a clearing event (YES) or not (NO). While we performed simulations over a total of four periods, the bulk of our analysis is focused on the Active #1 and Null #1 periods. However, the results for Active #2 and Null #2 periods are similar to the Active #1 and Null #1 periods, respectively.

2.3 Reanalysis Temperature Comparison

In order to increase our confidence in our simulations from WRF, we compared the diurnal cycle between ERA–Interim, ERA5 (ECMWF Reanalysis 5th Generation; Hersbach and Dee 2016), and MERRA2 (Modern-Era Retrospective analysis for Research and Applications, Version 2; Gelaro et al. 2017) with the diurnal cycle from WRF for the active #1 period. Figure 2.4 shows the diurnal cycle for each dataset. Overall, the diurnal cycle seems to be similar for all four datasets. The reanalyses (in particular MERRA2 and ERA5) seem to have a slightly warmer afternoon maximum than WRF, however, the daily minimum temperature between each dataset appears to be similar. The average minimum temperature for WRF was 286.1 K, 288.2 K for ERA–Interim, 287.2 K for ERA5, and 285.4 K for MERRA2.

Active #1		Active #2		Null #1		Null #2	
20 May 2013	YES	22 May 2014	NO	21 May 2008	NO	01 May 2009	NO
21 May 2013	NO	23 May 2014	YES	22 May 2008	NO	02 May 2009	NO
22 May 2013	YES	24 May 2014	YES	23 May 2008	NO	03 May 2009	NO
23 May 2013	NO	25 May 2014	YES	24 May 2008	NO	04 May 2009	NO
24 May 2013	YES	26 May 2014	YES	25 May 2008	NO	05 May 2009	NO
25 May 2013	YES	27 May 2014	YES	26 May 2008	NO	06 May 2009	NO
26 May 2013	YES	28 May 2014	YES	27 May 2008	NO	07 May 2009	NO

Table 2.1. Dates and clearing event characteristic (“yes”, “no”, “maybe”; see text for full description) of each simulation. Greyed shading indicates dates not analyzed to account for spin-up.

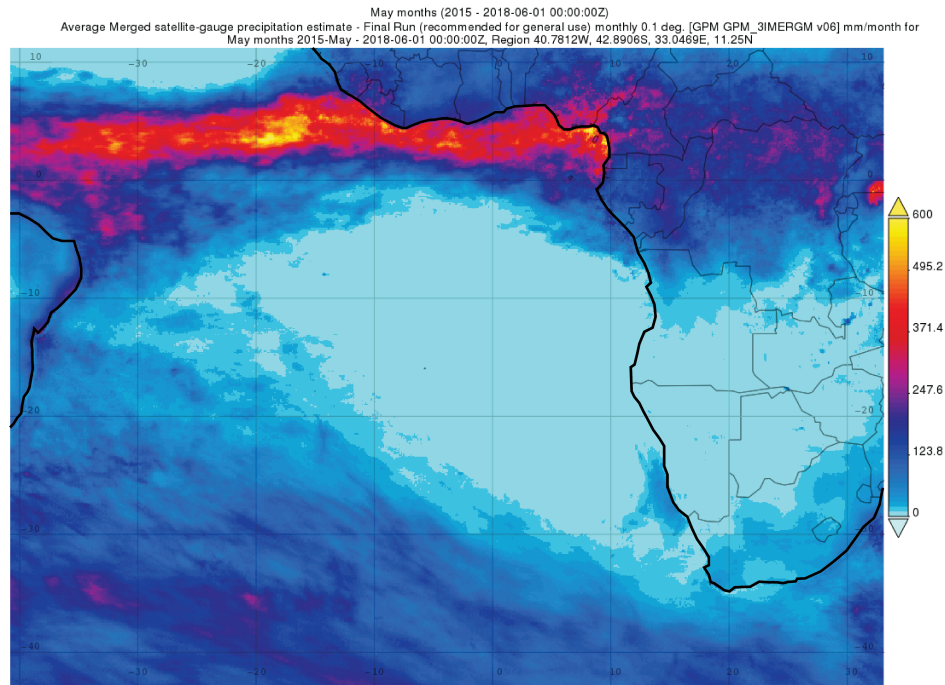


Figure 2.1. Precipitation from GPM for May 2015-2018 [mm/months]

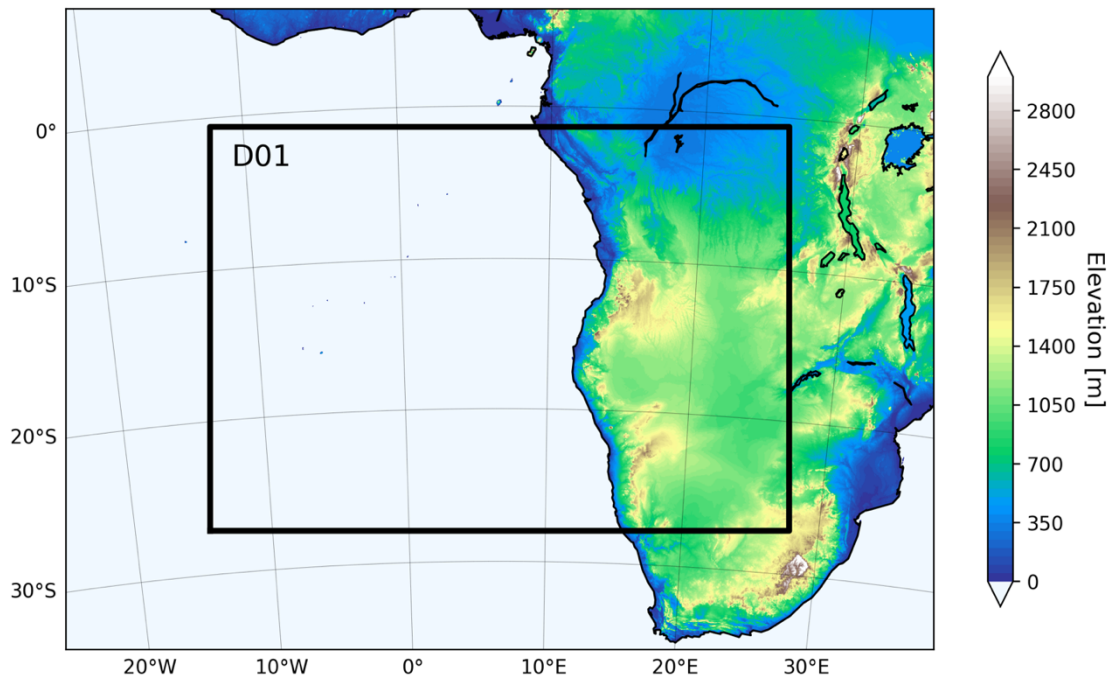


Figure 2.2. WRF domain configuration for the simulations with terrain (m; contoured every 50 m). Mesh D01 (black box) has horizontal grid spacing of 10 km. Fine mesh simulations with grid spacing 3.33 km have been performed but are not included in this report or on this figure.

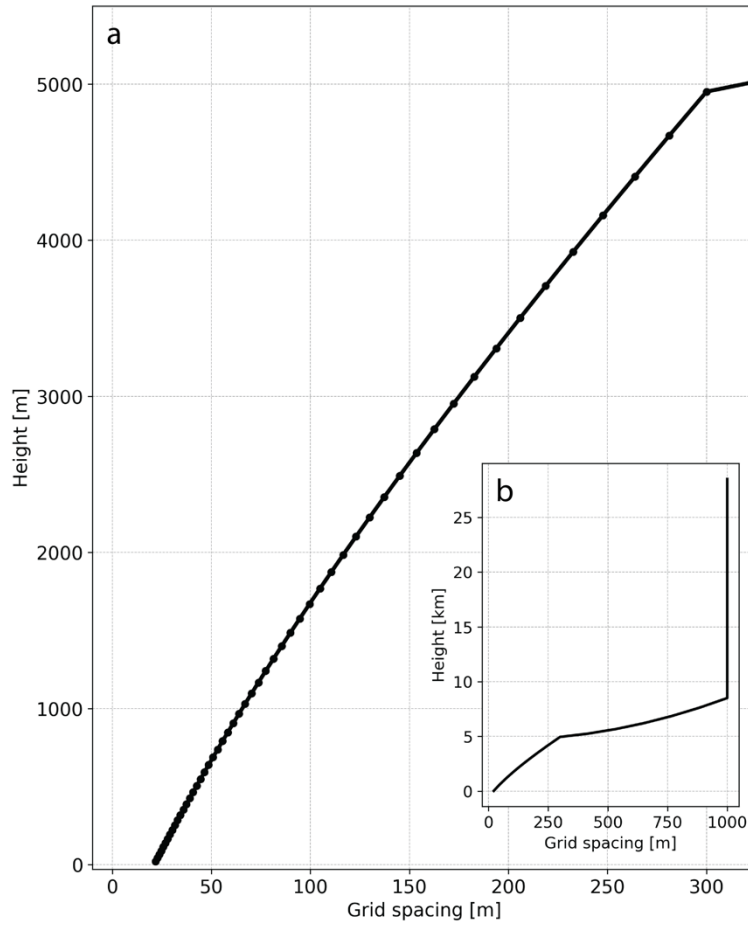


Figure 2.3. Vertical grid spacing in the model as a function of height for (a) lower 5 km and (b) full model vertical extent.

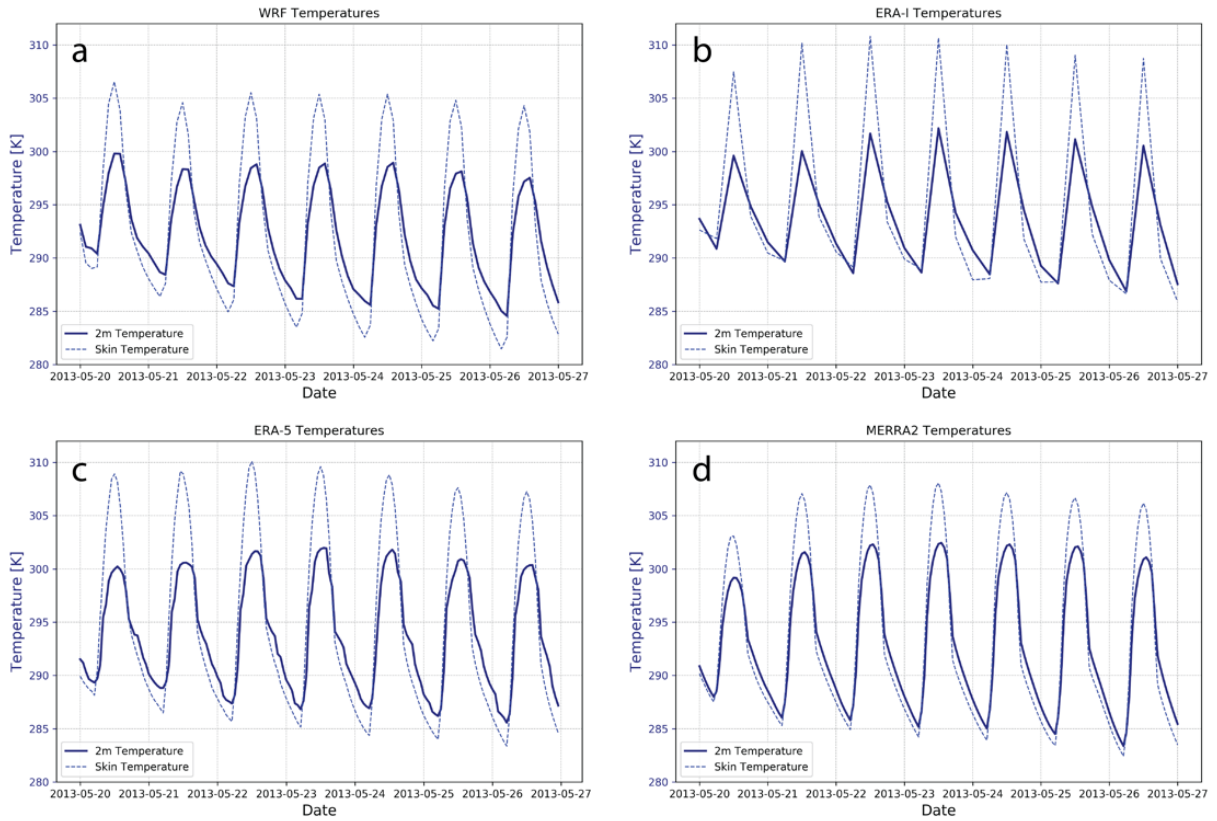


Figure 2.4. Diurnal cycle for (a) WRF, (b) ERA–Interim, (c) ERA5, and (d) MERRA2 data valid for 20 May 2013 0000 UTC to 27 May 2013 0000 UTC. 2-m temperatures (blue solid line) and skin temperatures (blue dashed line) are averaged over 15–20°S, 15–20°E.

CHAPTER 3 Results

3.1 Synoptic Overview

The domain of our simulations lies largely in the subtropics, extending into the tropics and midlatitudes in the northern and southern part of the domain, respectively (Fig. 2.2). Figure 3.1 shows the 500 hPa, 700 hPa, 900 hPa, and sea level pressure (SLP) analysis for two times during the active period early in the simulation but after the spin-up period (21 May 2013 0000 UTC), and at a time in the middle of the simulation (24 May 2013 0000 UTC). Note that the local time over the western portion of the WRF domain is the same as UTC, whereas east of 7.5°E, the local time is UTC+0100. In this study, we consider UTC to be at or near the local time. As is discussed in the sections above, the surface is largely dominated by a semi-permanent high pressure over the ocean due to the descending branch of the Hadley cell circulation and the cool ocean (Figs. 3.1g,h). Additionally, during the austral autumn, high pressure also exists over the land. This pattern is often accompanied by a trough of low pressure along the coast. While these patterns are the norm for the region in May, there are several differences in the synoptic features between the active and null periods.

Boundary layer depth increases away from the coast, with the active period ranging roughly from a pressure level of ~975 hPa near the coast (boundary layer height of ~250 m) up to ~925 hPa (boundary layer height of ~850 m) at 0° longitude. Above the boundary layer, high pressure generally prevails over the northern part of the domain, and lower pressure prevails in the southern part of the domain (Figs. 3.1a–f). Geopotential height fields in the free troposphere display greater variation of structure than does the surface pressure and baroclinic waves pass through the region to the south, which influence the surface pressure patterns.

An analysis of the 0000 UTC 21 May 500-hPa geopotential height field in the active period shows a trough over the southern part of the domain around 25°S (annotated with a black dashed line in Fig. 3.1a). The trough rapidly moves to the east and by 0000 UTC 24 May is no longer visible. After the wave passes through, a closed area of high pressure develops, centered along 15°S for the rest of the simulation (Fig. 3.1b). Due to the location of the high pressure, the flow along the southern part of the coast is onshore, and the flow further north between 10°S and 15°S is offshore. Similarly, Fig. 3.1c shows lower 700-hPa heights early in the simulation, transitioning to higher values and offshore flow towards the end of the simulation (Fig. 3.1d).

The flow at 900 hPa (~1 km AGL) is much more complex than originally anticipated. We expected the flow patterns to be similar to that of the surface wind patterns and largely controlled by the subtropical high pressure that is apparent in the SLP analysis (Figs. 3.1g,h). At 900 hPa (Fig. 3.1e), a low centered around 20-25°S, 5-10°E appears to be associated with the mid-level trough that passes through the region (Fig. 3.1a). An animation of the 900-hPa geopotential heights (Animation 3.1; see Appendix B for more information on animations) shows that the low meanders to the south and then weakens in the first 48 hours. It then moves to the north-northwest, likely advected by the low-level flow, where it then settles around 15°S, 5°E and strengthens slightly (Fig. 3.1f) before eventually becoming ill-defined in the last 48 hours of the simulation (Animation 3.1). In contrast, the SLP is not as variable as the upper levels, with the exception of a small low pressure centered around 25°S, 10°E at the beginning of the simulation associated with the mid-level disturbance (Fig. 3.1g).

In contrast to the active period, Fig. 3.2 shows the 500 hPa, 700 hPa, 900 hPa, and SLP analysis for two times during the null period at the beginning of the simulation after the spin-up period (22 May 2008 0000 UTC) and at a time in the middle of the simulation (25 May 2008

1600 UTC). The 500-hPa analysis shows low pressure towards the south of the domain (Fig. 3.2a) with waves propagating through the south in the middle of the simulation (Fig. 3.2b). A high in the northwest part of the region out over the ocean in combination with the low to the south is associated with onshore flow for the majority of the coastline. The 700-hPa field (Figs. 3.2c,d) exhibits greater variability than the 500-hPa heights but also indicates mostly onshore flow (especially between 10°S and 15°S; Fig. 3.2d). Initially, the 900-hPa analysis (Fig. 3.2e) shows a large high over the ocean and lower heights along the coast but as the simulation progresses, a low forms over the ocean, with accompanying strong onshore flow (Fig. 3.2f). Animation 3.2 indicates that this low forms from the trough along the coast, possibly thermally induced as the offshore flow advects warm air from the continent. This explanation requires a column of warm air to move off the continent, which creates height falls in the lower parts of the column and height rises in the upper parts of the column. The SLP analysis (Figs. 3.2g,h) shows a strong high pressure over the ocean and land as expected.

In the mid-levels, the active period has noticeably higher heights than in the null period (Figs. 3.1a–f, 3.2a–f). Additionally, at the surface, the active period has higher pressure, particularly over land (Figs. 3.1g,h, 3.2g,h). Disturbances in each period have differences in the formation, movement, and location. In the active period, the 900-hPa low (and the surface low) that forms to the south appears to be synoptically forced and then advected north-northwest by the low-level flow (Figs. 3.1e,f). However, during the null period, the low seems to form from a disturbance along the coast and is not associated with any obvious mid-level forcing (Animation 3.2). The low in the active period also remains further offshore than in the null period, seeming to have less of an impact on the flow along the coast (comparing Figs. 3.1e,f and 3.2e,f). The mid-level flow along the coast may also be an important difference between the null and active

periods, as the flow is mostly onshore during the null period (Figs. 3.2a–d) and more offshore in the active period (Figs. 3.1a–d). Animations of these fields (not shown) provide additional support for these ideas since Figs. 3.1 and 3.2 only show two times from each period. Further discussion and analysis of the offshore and onshore flow are presented in the next section.

3.2 Offshore Flow

3.2.1 900-hPa flow

Figure 3.3 shows Hovmöller diagrams of u , v , and w at 900 hPa for the active period averaged over a latitude band of 15°S to 20°S and a longitude range from 0°E to 15°E (shown in the red box in Fig. 3.2f). Figure 3.4 shows the same but for the null period. Both the active and null periods exhibit a clear diurnal signal in all three wind components. In the afternoon, the land warms up more than the ocean, and the pressure field responds accordingly. The increase in pressure gradient induces an onshore flow, whereas the reverse is true overnight when the land cools and the flow is accelerated from the land to the ocean. Figures 3.3a and 3.4a clearly show this signal near the coast with positive u in the afternoon and a negative u after midnight. There is also a diurnal signal in the v near the coast which shows a slightly negative (northerly) component for a few hours after midnight (Figs. 3.3b, 3.4b). The evolving pressure gradient associated with the diurnal cycle also results in an increase in the coastal jet speed during the afternoon and a slow-down overnight via geostrophic adjustment of the diurnally varying pressure gradient (i.e., the Coriolis-turning of the onshore or offshore flow accelerated by the diurnally varying pressure gradient force). Finally, the diurnal cycle in the w near the coast shows upwards motion during the afternoon and evening and downward motion after midnight consistent with the terrestrial heating and cooling patterns (Figs. 3.3c, 3.4c).

The diurnal cycles in both periods are consistent with our expectations of coastal dynamics (Garreaud and Muñoz 2005); however, several differences between the two periods are noted. The u Hovmöller diagrams for the active period (Fig. 3.3a) appear to show broader areas of overnight offshore flow near the coast compared to the null period (Fig. 3.4a). With the exception of the large-scale onshore flow during the first 48 hours of the active period, the areas of afternoon onshore flow in the active period are much weaker and span over a smaller area than in the null period. In contrast, the overnight offshore flow in the null period is weaker than the active period. The onshore flow in the null period extends as far out at 4°E on 27 May and reaches a strength of at least 5 m s^{-1} (Fig. 3.4a) whereas the onshore flow in the active period does not extend beyond the coast at 12°E and only reaches a strength of about 2 m s^{-1} (Fig. 3.3a).

Both periods have regions of northerly flow shown in the v Hovmöller diagrams (Figs. 3.3b, 3.4b). In the active period, the northerly flow is centered more offshore around 8°E (moving west to 5°E ; Fig. 3.3b) whereas in the null period, the northerly flow is directly offshore hovering around 10°E and eventually extending westward to 4°E later in the simulation (Fig. 3.4b). These regions of northerly flow are associated with the lows at 900 hPa like those shown in Figs. 3.1f and 3.2f. Animations 3.1 and 3.2 show the spatial detail of these northerly coastal flows present in the Hovmöller diagrams.

The “slanted” features in the u and v Hovmöller diagrams (Figs. 3.3a,b) from the active period indicate a westward propagation of the wind features. The slope of these lines corresponds to a propagation speed of $\sim 10 \text{ m s}^{-1}$. This finding is not particularly helpful in identifying the propagation mechanism since the speed is close in magnitude to the large-scale flow (advection), a range of internal gravity-wave phase speeds, and the motion of the cloud-

eroding boundary itself (Yuter et al. 2018). It is important, however, that these propagating features are not present in the null period.

Differences in the vertical motion between the active and null periods are slightly more subtle than in the u and v Hovmöller diagrams. First, the downward motion over land at night in the null period is much weaker than in the active period, while the upward motion during the day over land is of similar magnitude in both periods (Figs. 3.3c, 3.4c). A detailed comparison between the diurnal temperature variation over land in the two periods indicates that this difference in magnitude is not due to differences in overnight cooling (see Appendix C for a full analysis). However, we speculate that because the active period has stronger offshore flow overnight, then this may force a stronger response in the downward vertical motion over land (Fig. 3.3). The second difference present in the Hovmöller diagrams of vertical motion is a wave-like feature of upwards and downwards motion propagating westward (offshore) in the active period (Fig. 3.3c). The feature leaves the coast just before 0000 UTC and moves out to 6°E almost a day later. This feature is not present in the null period (Fig. 3.4c).

3.2.2 900-hPa Geostrophic flow

Figures 3.5 and 3.6 show the u and v components of the wind broken down into the geostrophic and ageostrophic components for the active and null periods, respectively. The total wind is partitioned into geostrophic and ageostrophic components as in Eq. (1). The geostrophic wind is calculated using Eq. (2) from Holton (2004), and the ageostrophic wind is calculated by subtracting the geostrophic wind from the total wind.

$$\vec{V} = \vec{V}_g + \vec{V}_a \quad (1)$$

$$\vec{V}_g = \frac{1}{f} \hat{k} \times \nabla \Phi \quad (2)$$

Note that some data are missing from these ageostrophic Hovmöller diagrams because a Gaussian filter was applied to the geopotential heights before calculating the geostrophic wind, which caused some contamination of the data over the land. Comparing the geostrophic/ageostrophic components in Figs. 3.5 and 3.6 to the full wind fields in Figs. 3.3 and 3.4 show that the overall flow is largely dictated by the geostrophic component of the flow (which is expected). The ageostrophic components can be thought of as acceleration. Figure 3.5b indicates that near the coast the u is accelerating towards the land in the afternoon which is consistent with the diurnal cycle of the coastal jet. As the land heats up, the pressure gradient strengthens and the air accelerates towards the land. Figure 3.5d indicates a positive ageostrophic v (southerly acceleration) in the evening through the morning and a negative ageostrophic response in v (northerly acceleration) in the afternoon. This is likely a response to the changing pressure gradient since at night the pressure gradient will weaken (as the land cools down), and the geostrophic v will decrease but the total wind has not yet, so the ageostrophic v will be positive (southerly acceleration). Similarly, in the null period, Fig. 3.6b shows the ageostrophic u has a positive component (westerly acceleration) during the day until 0000 UTC, which we would expect given the heating during the day. The positive ageostrophic u feature extends a substantial distance offshore (as far out to 5°W on some days, not shown), which indicates that the diurnal effects from the terrain can force a response in the coastal jet fairly far out over the ocean. The considerable westward extent of the jet's response to the pressure gradient is not well understood and will require additional work. Additionally, Hovmöller diagrams at 800 hPa and 950 hPa show similar patterns indicating that these features are not only present at 900 hPa (see Appendix D).

These patterns are also seen in Hovmöller diagrams of u for the ERA–Interim data for each the active and null periods, shown in Figs. 3.7 and 3.8, respectively. Figure 3.7a shows similar patterns of offshore and onshore flow when compared to the WRF u Hovmöller diagram for this period (Fig. 3.3a). Additionally, the geostrophic and ageostrophic wind features in Figs. 3.7b,c are similar to those in Figs. 3.5a,b. However, the ERA–Interim Hovmöller diagrams do not exhibit any westward propagating features like the WRF ones do. Additionally, the ERA–Interim data is every 6 hours, which produces much coarser features than in the WRF data (which is output every hour). Similarly, Fig. 3.8a shows similar patterns compared to the WRF data for the same period in Fig. 3.4a. The geostrophic and ageostrophic patterns in the ERA–Interim Hovmöller diagrams are also similar to Figs. 3.6a,b. In particular, the ERA–Interim ageostrophic u Hovmöller diagrams in Fig. 3.8c show the striped features in Fig. 3.6b. This behavior is not understood but is clearly seen in the ERA–Interim data as well as in the WRF model. Satellite derived surface winds may be helpful in understanding the physical mechanisms governing these ageostrophic components.

3.2.2 Surface flow

The 10-m wind patterns within the boundary layer are similar for both the active and the null periods. In the afternoon, the 10-m u Hovmöller diagrams show mostly offshore wind, with localized areas of weak onshore wind near the coast (Figs. 3.9a, 3.10a). The 10-m v Hovmöller diagrams indicate predominantly southerly flow (Figs. 3.9b, 3.10b). This southerly flow is consistent with the wind patterns shown in the SLP analysis in Figs. 3.1 and 3.2 and the climatological flow over this region. However, there are differences in the magnitude of the 10-m flow between the active and null periods. In the null period, the flow is about $1\text{--}2\text{ m s}^{-1}$ stronger both in the u and the v (Figs. 3.10a,b). Figures 3.9c and 3.10c show Hovmöller diagrams

of SLP, which indicate that the active period has higher pressure both over the land and the ocean consistent with the synoptic analysis presented in Figs. 3.1g,h and 3.2g,h. The active period also appears to have a stronger pressure gradient (particularly between 12°E and 14°E) compared to the null period (Figs. 3.9c, 3.10c).

3.2.3 Cross sections

Figure 3.11 shows cross sections over a 12-hour period along 15°S (along the blue line in Fig. 3.2f). The sequence of images begins at 1400 UTC on 22 May 2013 and progresses every 4 hours until 0400 UTC on 23 May 2013. Details of the features are best seen in the hourly images of panels (a)–(d) from Fig. 3.11 in Animation 3.3. This time period includes flow features which are present almost every night of the simulation, but this time period is one of the clearest examples. Figure 3.11a–d show cross sections of w and u . The boundary layer height is also shown with a solid black line. Boundary layer heights were calculated by finding gradients in vertical profiles of potential temperatures. The lowest height between 200 m and 5000 m that has a potential temperature gradient exceeding 1.5 K / 100 m designates the boundary layer height. We note that models consistently underestimate boundary layer heights (Wyant et al. 2015), so while we do not necessarily trust the exact boundary layer heights shown here we do have confidence in the relative boundary layer heights between the two periods. At the beginning of the period, areas of strong upward motion can be seen over the land and near the coast associated with the heating of the land during the day (Fig. 3.11a). In the late afternoon, some of this upward motion appears to move further inland, likely advected by the onshore flow (Fig. 3.11b,j). Around 2000 UTC, part of the larger area of upward motion begins to move away from the land out over the ocean (Fig. 3.11c). This area of upward motion has a maximum intensity between 500 and 1000 m and remains above the boundary layer. This area is also coupled with a

local maximum in the u field, indicating that this area is not moving due to advection but rather is propagating against the flow (Fig. 3.11j,k). It moves out to $\sim 9^\circ\text{E}$ at 0400 UTC before dissipating. This coupled upward and westward propagation appears very wave-like and qualitatively similar to upsidence waves documented over the SEP by Garreaud and Muñoz (2004), O'Dell et al. (2008), and Rahn and Garreaud (2010). Cross sections of temperature (Figs. 3.11e–h) show that the air that moves offshore over the boundary layer overnight is warmer than the air within the boundary layer. The overrunning air from the continent would increase the shear at the top of the boundary layer and possibly increase the entrainment of warm dry air into the cloud.

Figure 3.12 shows a similar panel of images in Fig. 3.11 but for the null period. Animation 3.4 shows hourly images of panels (a)–(d) in Fig. 3.12 through this period. The propagating upward motion feature above the boundary layer in the active period discussed in the previous paragraph is not present in the null period (Figs. 3.12a–d). However, in the null period, an area of downward motion appears to move offshore throughout this period but is further above the boundary layer, ~ 2 km above ground level (AGL). Additionally, Figs. 3.12e–h show that the air above the boundary layer is warmer than the air within the boundary layer; however, the air is slightly cooler in the null period than in the active period (Figs. 3.11e–h).

3.2.4 Tracer fields

Figure 3.13 shows plan views (a,b) and cross sections (c,d) of two realizations of a passive tracer field initialized over land at the beginning (after first 24 hours) and end (at the last hour) of the active period. The passive tracer field was added to the model using the method of Blaylock et al. (2017). The scalar tracer field is unitless and is initialized at the beginning of the simulation and is updated every time step with a value of unity. This then acts as a tracer source as the field

is advected away from the source region. The tracer field is initialized in the first six vertical levels of the model, up to around 160 m AGL, and cover an area of 22 x 23 grid points (220 km x 230 km). One tracer region is placed over land near the coast (12°E to 15°E, 15°S to 17°S) to visualize the flow patterns associated with the land-sea breeze circulation. The tracer field over land is initialized at an elevation between 200 m and 1500 m. Another tracer region is initialized over the ocean (9°E to 11°E, 15°S to 17°S) to see the flow patterns within the boundary layer. The plan views (Figs. 3.13a,b) show a quasi-integrated quantity of the tracer field by adding up the value of the tracer field in each column.

Animations 3.5 and 3.6 show movies of the tracer fields every hour during the active period. Initially, the tracer field remains mostly over the continent (Fig. 3.13a, Animations 3.5, 3.6) but as the simulation progresses, the tracer field is evident further out over the ocean eventually reaching as far out as 0°E (Fig. 3.13b). Figures 3.14a,b and animations 3.7 and 3.8 show the progression of the tracer field over land during the null period. The tracer field initialized over land remains mostly over the continent and does not move out over the ocean nearly as far as they do during the active period (Figs. 3.13a,b, animations 3.7, 3.8). Vertical cross sections show the tracer field being lofted up over the land during the day when the diurnal heating causes upward motion. The tracer field is lofted up to 6 km (~ 4.5 km AGL; Fig. 3.13c) but usually remains below 4 km (~2.5 km AGL; Fig. 3.13d, 3.14c,d). During the active period, the tracer field is advected westward during the overnight hours and remains above the boundary layer (Fig. 3.13d, Animations 3.5, 3.6).

The tracer field initialized in the marine boundary layer is mostly advected to the north and exhibits little east–west dispersion for either period (Figs. 3.15a,b, 3.16a,b), consistent with the anticyclonic flow at the surface and within the boundary layer. Within the first 24 hours of the

simulations, the tracer field has already reached 10°S (Figs. 3.15a, 3.16a). Because the tracer field does not penetrate through the top of the boundary layer, the plan views (Figs. 3.15a,b, 3.16a,b; which show a quasi-integrated quantity of the tracer) can be interpreted as boundary layer thickness (i.e., deeper boundary layers mean more tracer in the column and darker shading). This idea can help to identify any perturbations that move through the boundary layer and cause thickening of the boundary layer. Animations of these fields show “ripples” — likely internal gravity waves — that move along the top of the boundary layer in both periods (Animations 3.9, 3.11). Animations 3.10 and 3.12 show movies of the cross sections shown in Figs. 3.15c,d and 3.16c,d and also show these waves in the boundary layer height (seen both in the tracer fields themselves and in the calculated boundary layer height). The idea of darker shading being proportional to a deeper boundary layer also helps to compare the boundary layer height between the two periods. The shaded region in Animation 3.11 is much darker than in animation 3.9, which indicates that the boundary layer in the null period is deeper overall than the boundary layer in the active period. The deeper boundary layer is additionally confirmed in the cross sections (Figs. 3.15c,d, 3.16c,d) which show the calculated marine boundary layer height as a dashed line. The differences in boundary layer height are discussed more in the next section.

3.3 Boundary layer Height

Figure 3.17 shows a plan view of the boundary layer height (BLH) for a representative time in both the active (a) and null (b) period. This figure confirms the idea presented in the previous section and shows that the boundary layer height is lower in the active period than it is in the null period. Both periods have a low boundary layer height near the coast (~100–200 m) and then increasing with height moving west. This pattern matches the climatological patterns in

boundary layer height for this region. Where these two periods differ is in the boundary layer height away from the coast. In the null period, the height of the boundary layer rises above 1600 m in some areas, whereas the boundary layer height remains below 1000 m in the active period (Fig. 3.17a,b). Figure 3.17a also indicates that in the active period, the boundary layer height increases to the west until around 0°E when the height begins to level off decrease slightly to the west. Since boundary layer heights are often underestimated in models (Wyant et al. 2015), the absolute height differences here are not as important as the relative height differences between the two periods.

Hovmöller diagrams of BLH averaged over 15°S to 20°S, 0°E to 15°E shown in Fig. 3.18 also support the idea that the BLH is higher in the null period than in the active period. Close to the coast, the boundary layer is shallow and becomes deeper further west. At 0°E, the boundary layer height is only around 800 m for the active period (Fig. 3.18a) but above 1300 m for the null period (Fig. 3.18b). Figure 3.18b also indicates a noticeable diurnal signal in the boundary layer height in the null period.

Figure 3.19 shows the median boundary layer height averages over 15°S to 20°S between 5°W and 12°E both during the day (1400–1800 UTC) and overnight (0200–0600 UTC) for the active and null periods. The interquartile range is indicated by the shaded region. Over most of the longitudes, the boundary layer height is higher overnight than it is during the day. This figure again provides support that the boundary layer height is deeper in the null period than it is in the active period. Another notable feature is the gradient in boundary layer height with longitude away from shore, which is much smaller in the active period than it is in the null period.

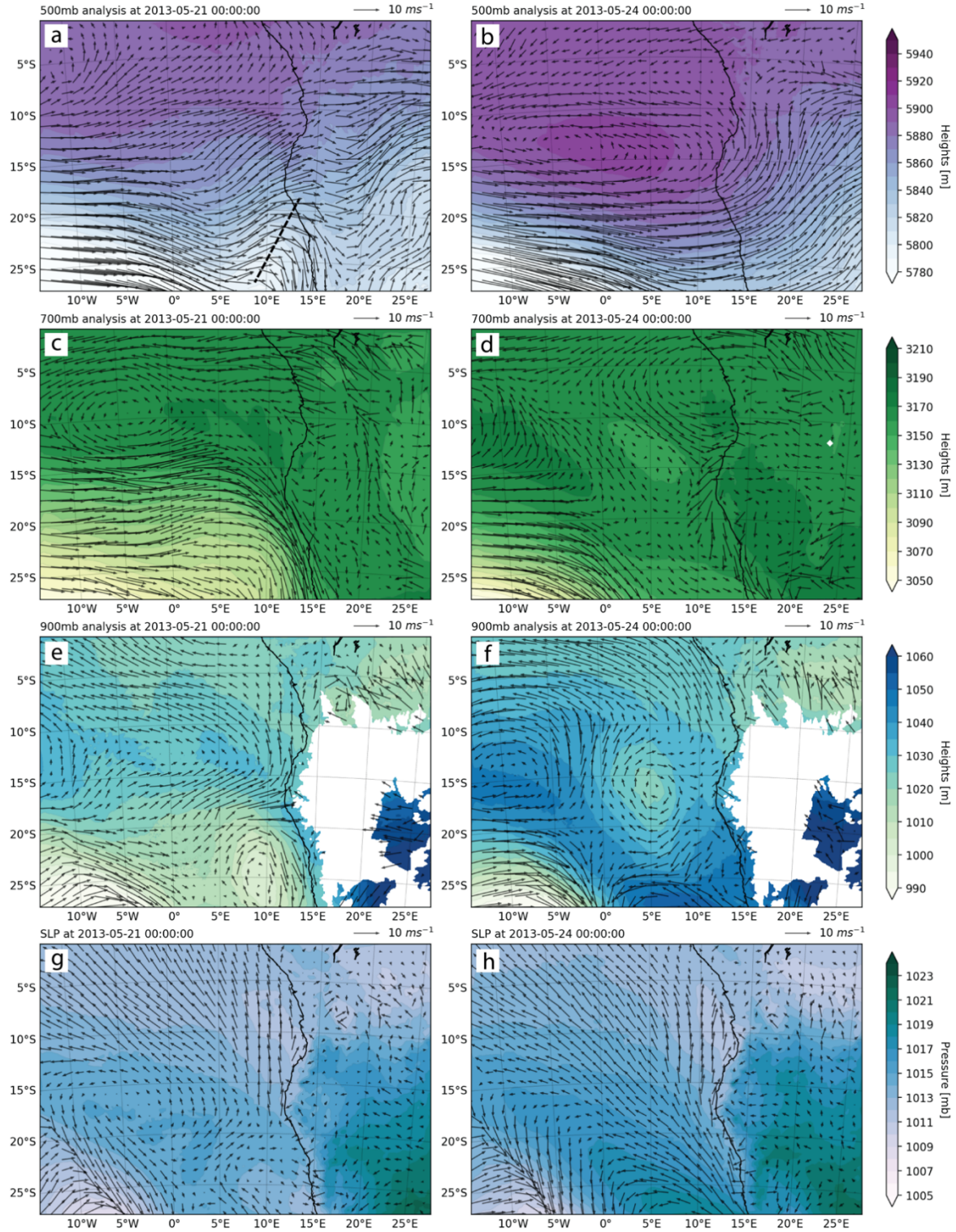


Figure 3.1. Simulated synoptic fields for two times during the active period (21 May 2013 0000 UTC [left column] and 24 May 2013 0000 UTC [right column]). (a) and (b) 500-hPa heights (m; contoured every 10 m) and wind (key in upper right). (c) and (d) 700-hPa heights and wind. (e) and (f) 900-hPa heights and wind. (g) and (h) SLP (hPa; contoured every 1 hPa) and 10 m winds. Black dashed line in panel (a) indicates the location of trough discussed in text.

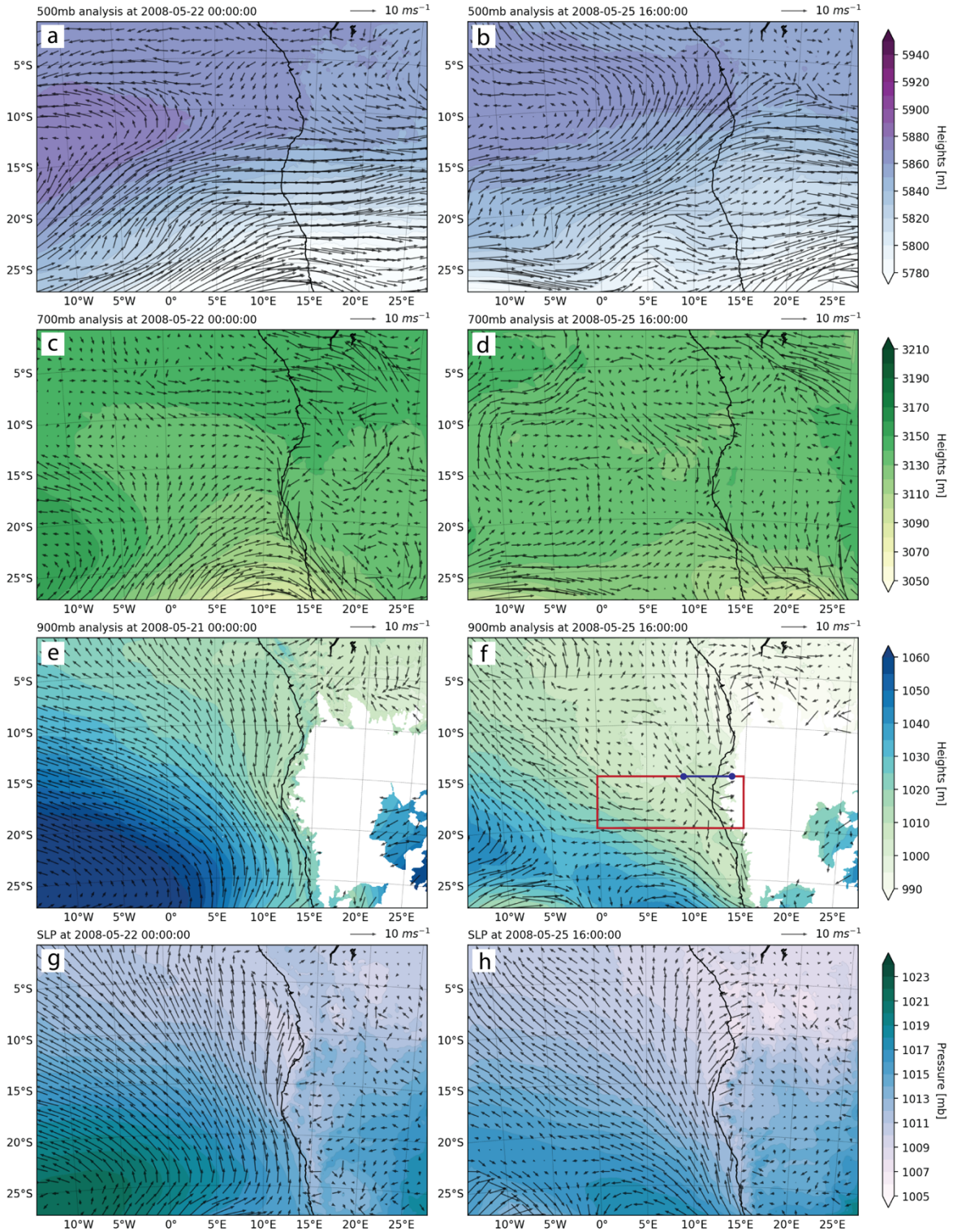


Figure 3.2. As in Fig. 3.1 but for two times during the null period. 22 May 2008 0000 UTC (left column) and 1600 UTC (right column). The red box in panel (f) indicates the area where Hovmöller diagrams are averaged over. The blue line in panel (f) indicates the location of cross sections.

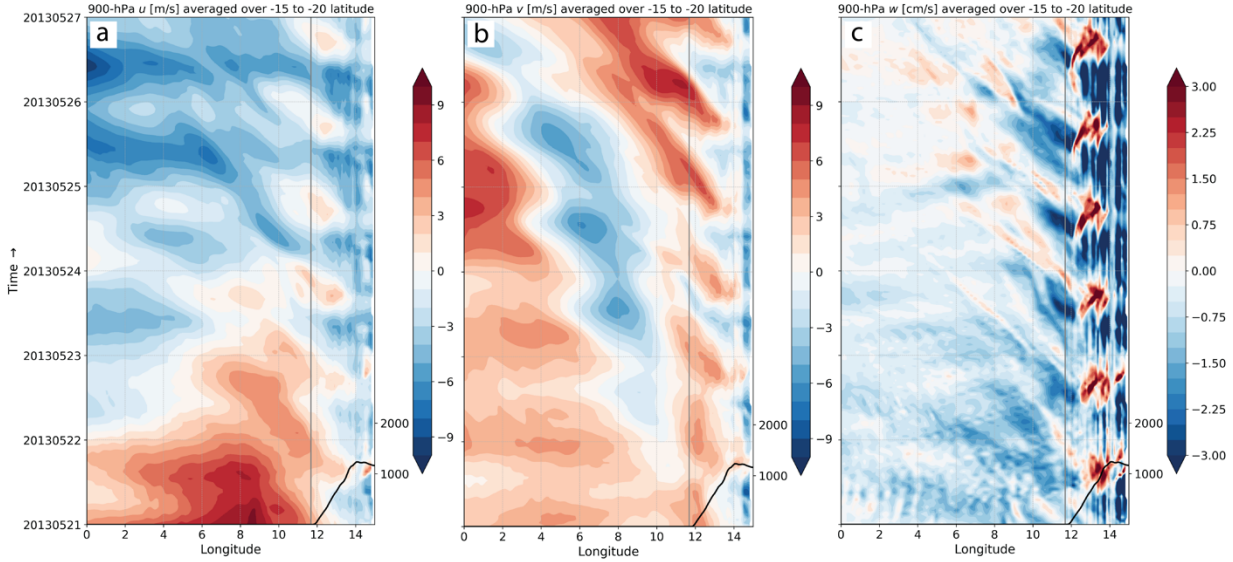


Figure 3.3. Hovmöller diagrams of 900-hPa (a) u (m s^{-1} ; contoured every 1 m s^{-1}), (b) v (m s^{-1} ; contoured every 1 m s^{-1}), and (c) w (cm s^{-1} ; contoured every 0.25 cm s^{-1}) during the active period. Hovmöller diagrams are calculated over the latitude range of 15°S to 20°S (red box in Fig. 3.2a). The black line in the bottom corner indicates the average coastline over this region and the bold grey line shows where the average coastline begins. Tick marks on y axis indicate time at 00 UTC.

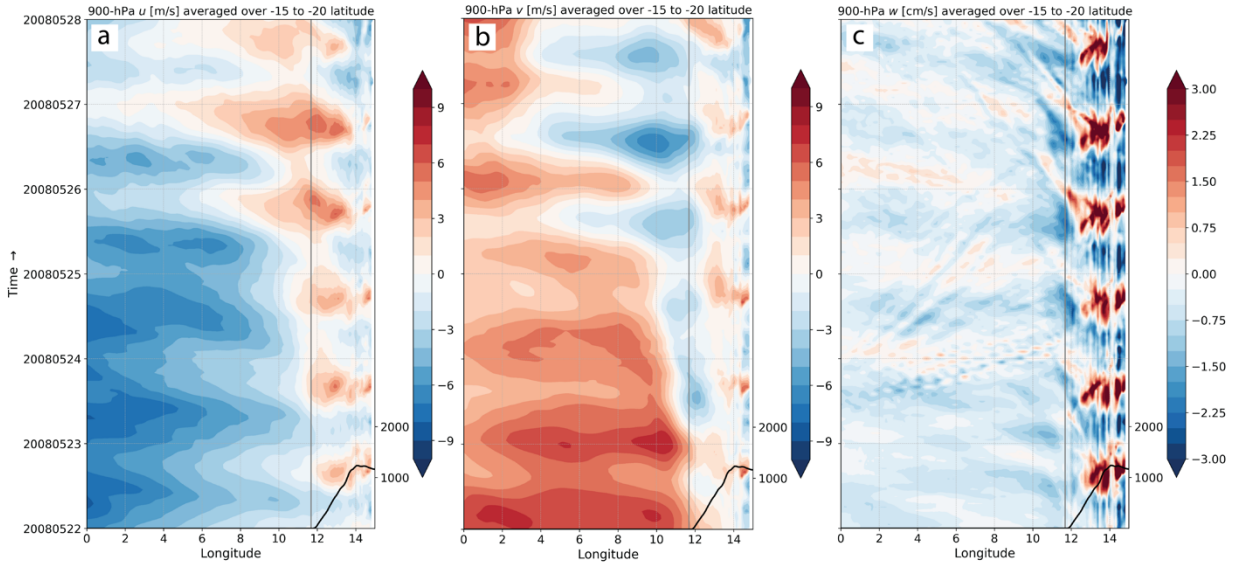


Figure 3.4. As in Fig. 3.3 but for the null period.

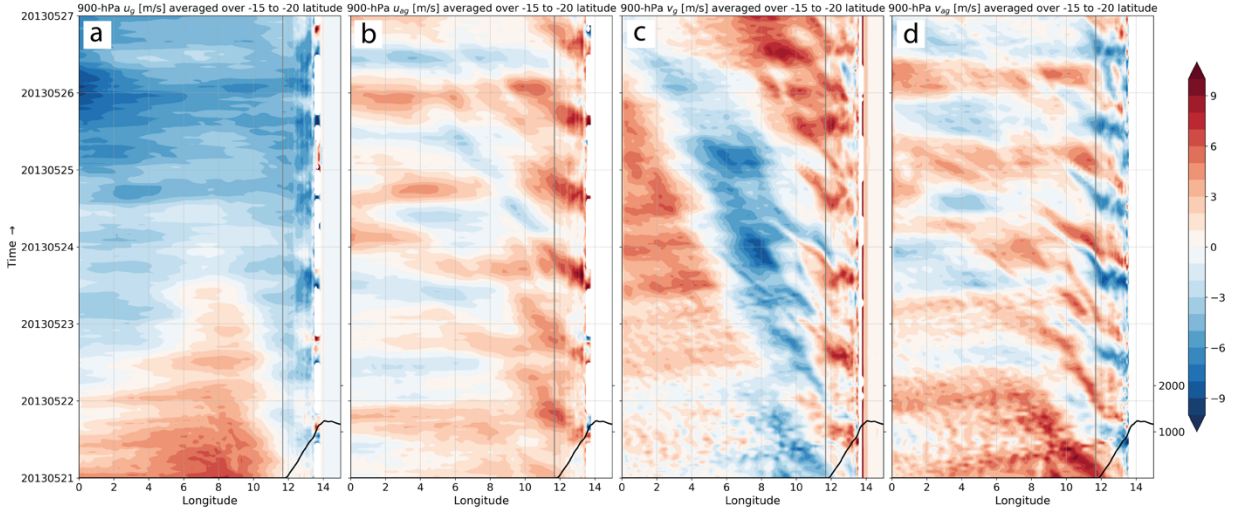


Figure 3.5. Hovmöller diagrams of the geostrophic and ageostrophic components of the 900-hPa wind components for the active period. (a) u_g , (b) u_a , (c) v_g , (d) v_a (m s^{-1} ; contoured every 1 m s^{-1}). As in Figs. 3.3 and 3.4, Hovmöller diagrams are calculated over the latitude range of 15°S to 20°S (red box in Fig. 3.2a). The black line in the bottom corner indicates the average coastline over this region and the bold grey line shows where the average coastline begins. Tick marks on y axis indicate time at 00 UTC.

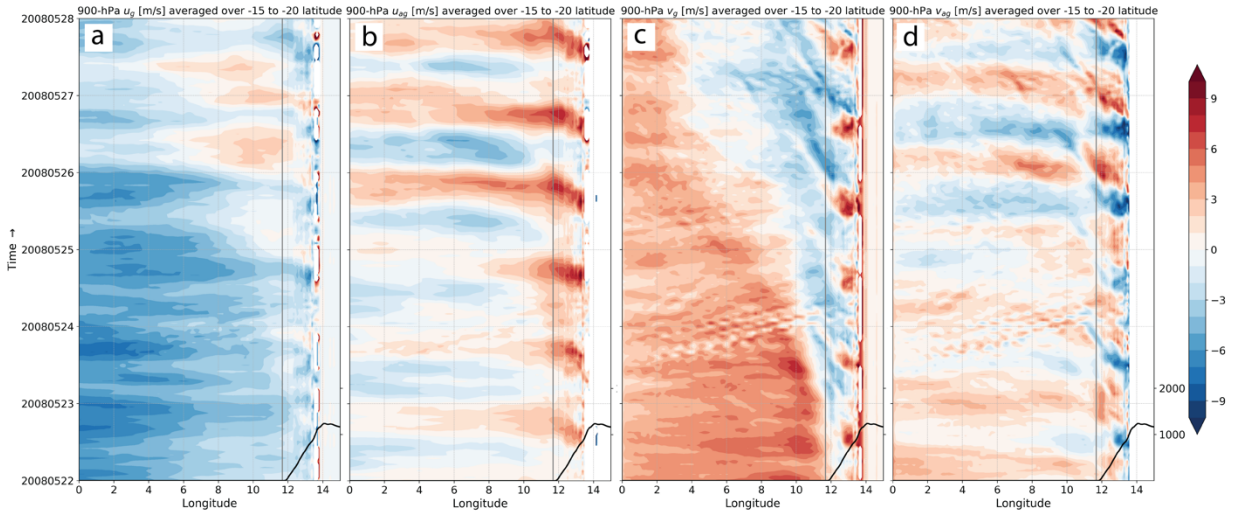


Figure 3.6. As in Fig. 3.5 but for the null period.

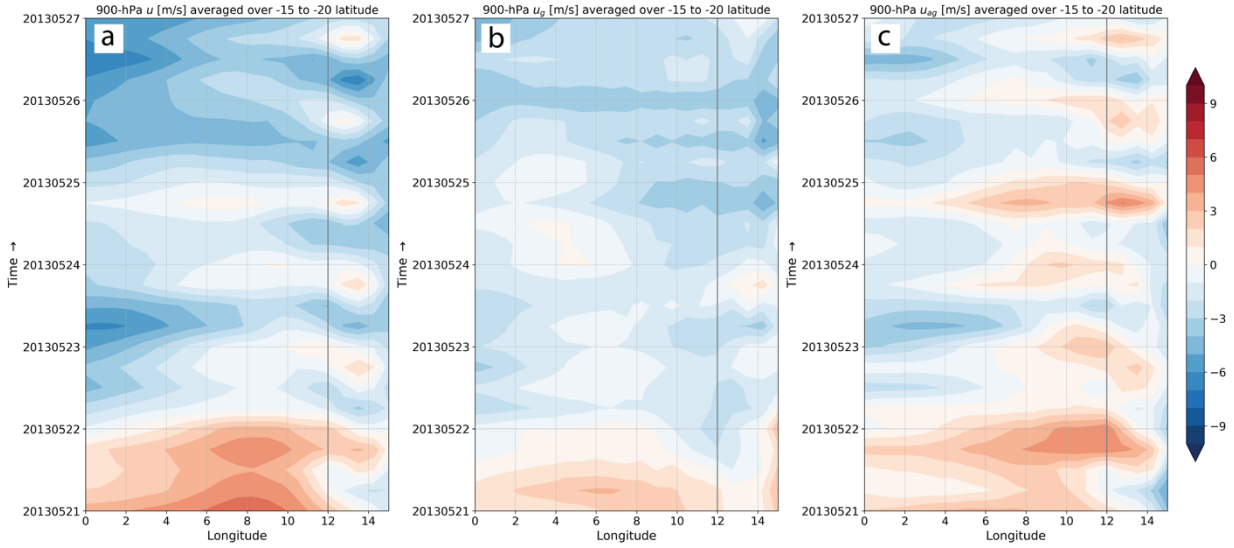


Figure 3.7. ERA–Interim Hovmöller diagrams of the geostrophic and ageostrophic components of the 900-hPa u wind components for the active period; (a) u , (b) u_g , and (c) u_a (m s^{-1} ; contoured every 1 m s^{-1}). Hovmöller diagrams are calculated over the latitude range of 15°S to 20°S (red box in Fig. 3.2a). The bold grey line indicates where the average coastline begins. Tick marks on y axis indicate time at 00 UTC.

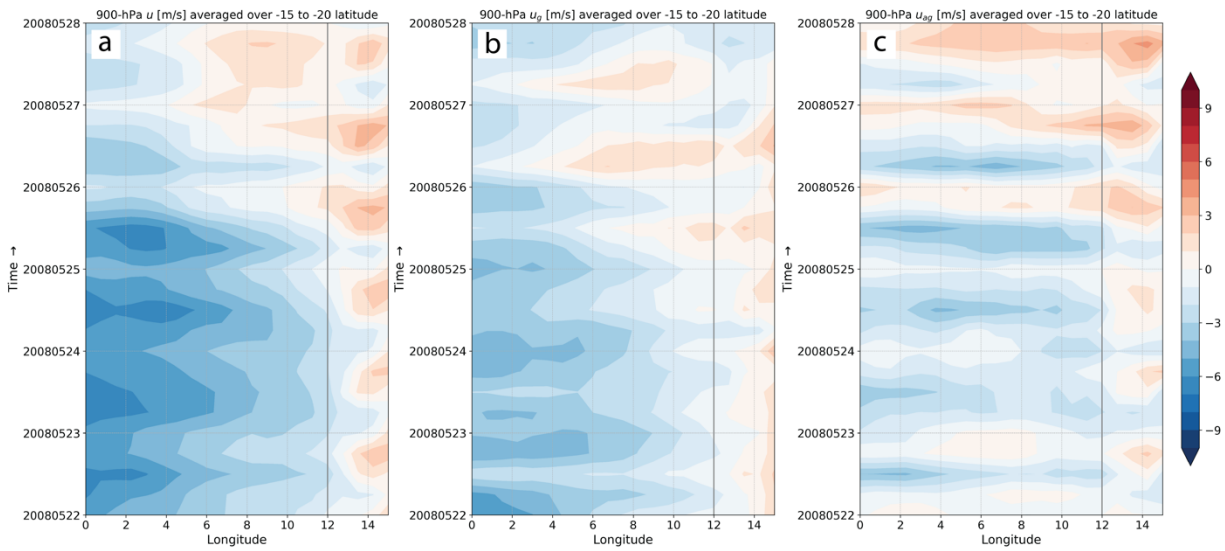


Figure 3.8. As in Fig. 3.7 but for null period.

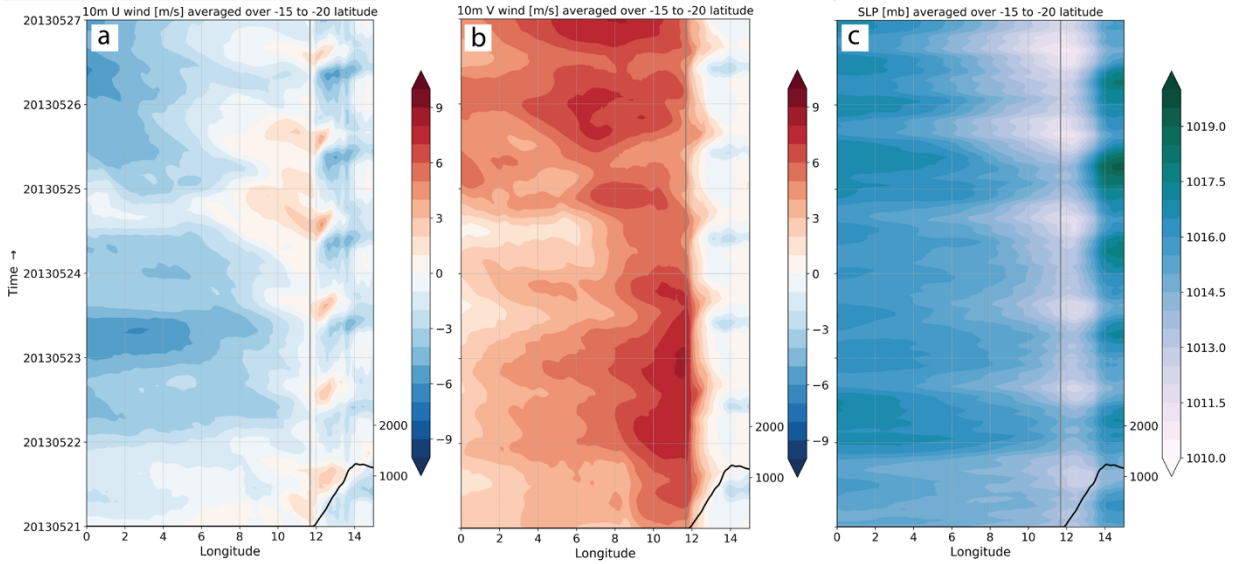


Figure 3.9. Hovmöller diagrams of (a) 10-m u (m s^{-1} ; contoured every 1 m s^{-1}), (b) 10-m v (m s^{-1} ; contoured every 1 m s^{-1}), (c) SLP (hPa; contoured every 0.5 hPa), calculated over the latitude range of 15°S to 20°S (red box in Fig. 3.2a). The black line in the bottom corner indicates the average coastline over this region and the bold grey line shows where the average coastline begins. Tick marks on y axis indicate time at 00 UTC.

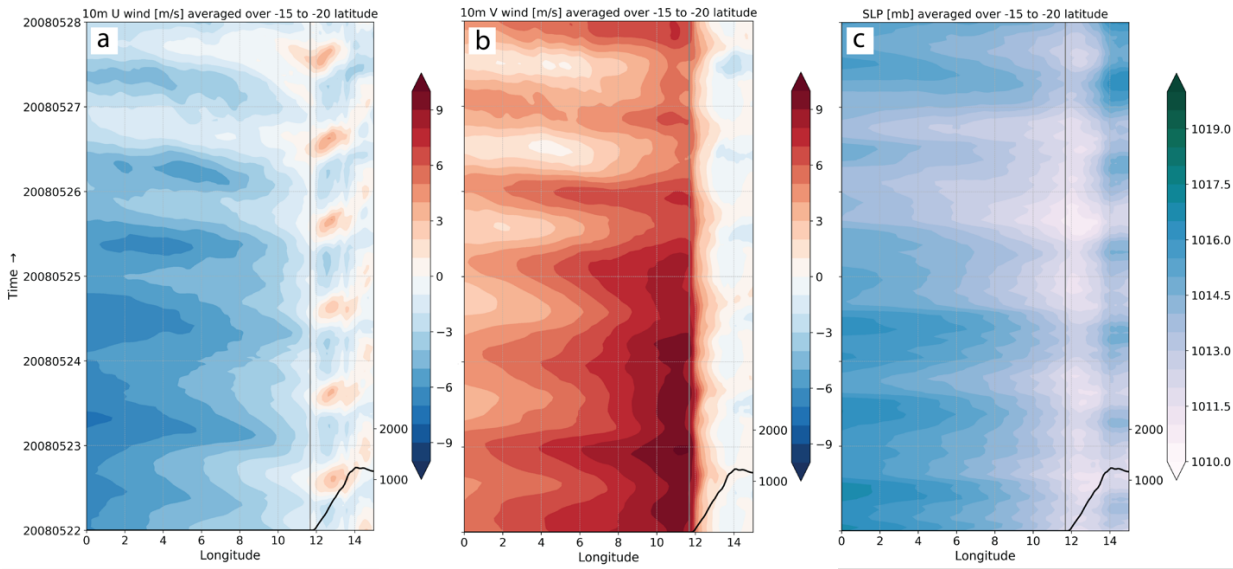


Figure 3.10. As in Fig. 3.9 but for the null period.

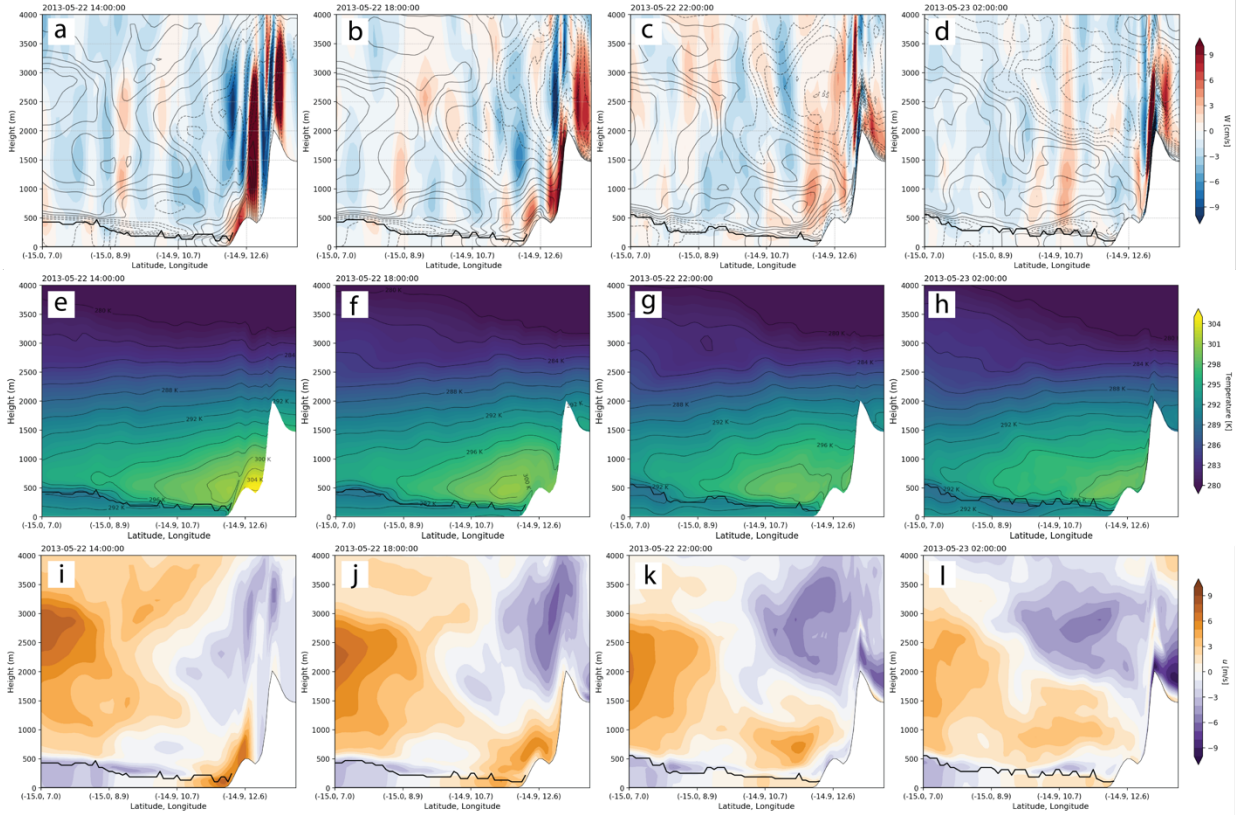


Figure 3.11. Cross section along 15°S (blue line in Fig. 3.2a) of (a)–(d) w (shaded; contoured every 1 cm s^{-1} ; red indicates areas of upward motion, blue indicates areas of downward motion), u (grey lines; contoured every 1 m s^{-1} , dashed indicates negative (easterly) values) and boundary layer height (BLH, bold black line), (e)–(h) Temperature (shaded; contoured every 1 K) and BLH (bold black line), (i)–(l) u (shaded; contoured every 1 m s^{-1} ; orange indicates positive (westerly) motion, purple indicates negative (easterly) motion) and BLH (bold black line), valid every 4 hours from 22 May 2013 1400 UTC to 23 May 2013 0200 UTC from the active period.

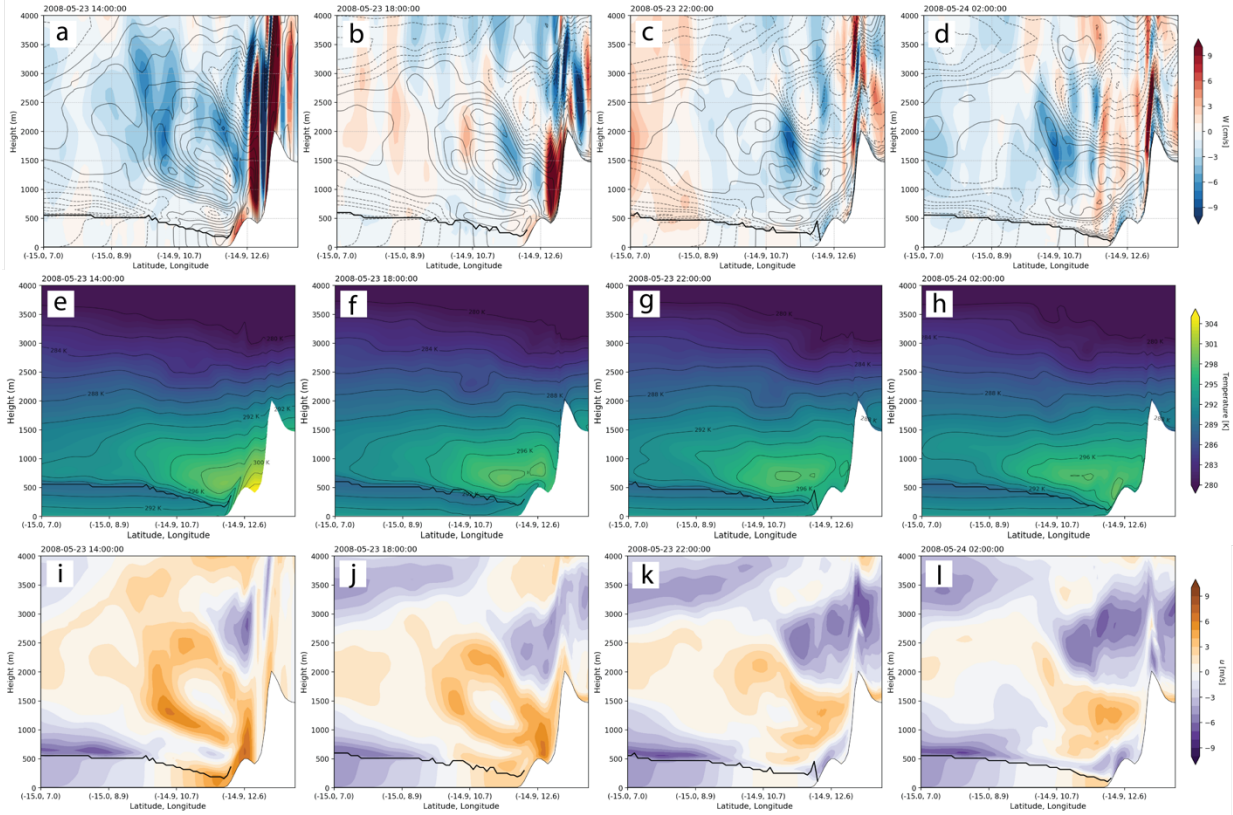


Figure 3.12. As in Fig. 3.11 but for the null period, valid every 4 hours from 23 May 2008 1400 UTC to 24 May 2013 0200 UTC.

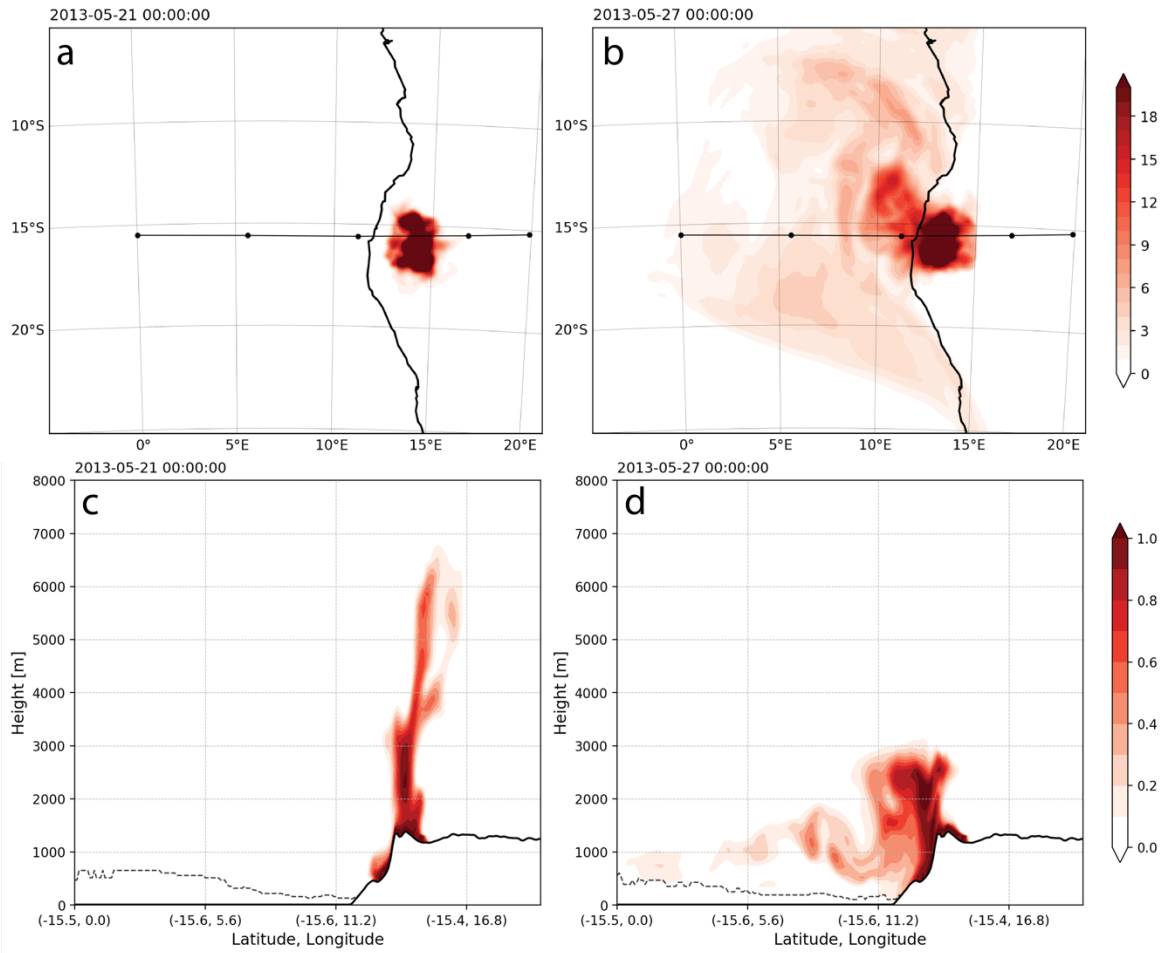


Figure 3.13. (a)–(b) Plan views of the simulated column-integrated ‘land’ passive tracer field (red shaded, dimensionless) for two times during the active period (21 May 2013 0000 UTC and 27 May 2013 0000 UTC). (c)–(d) Vertical cross section of tracer along 15.5°S line indicated in (a) and (b) and BLH (dashed black line).

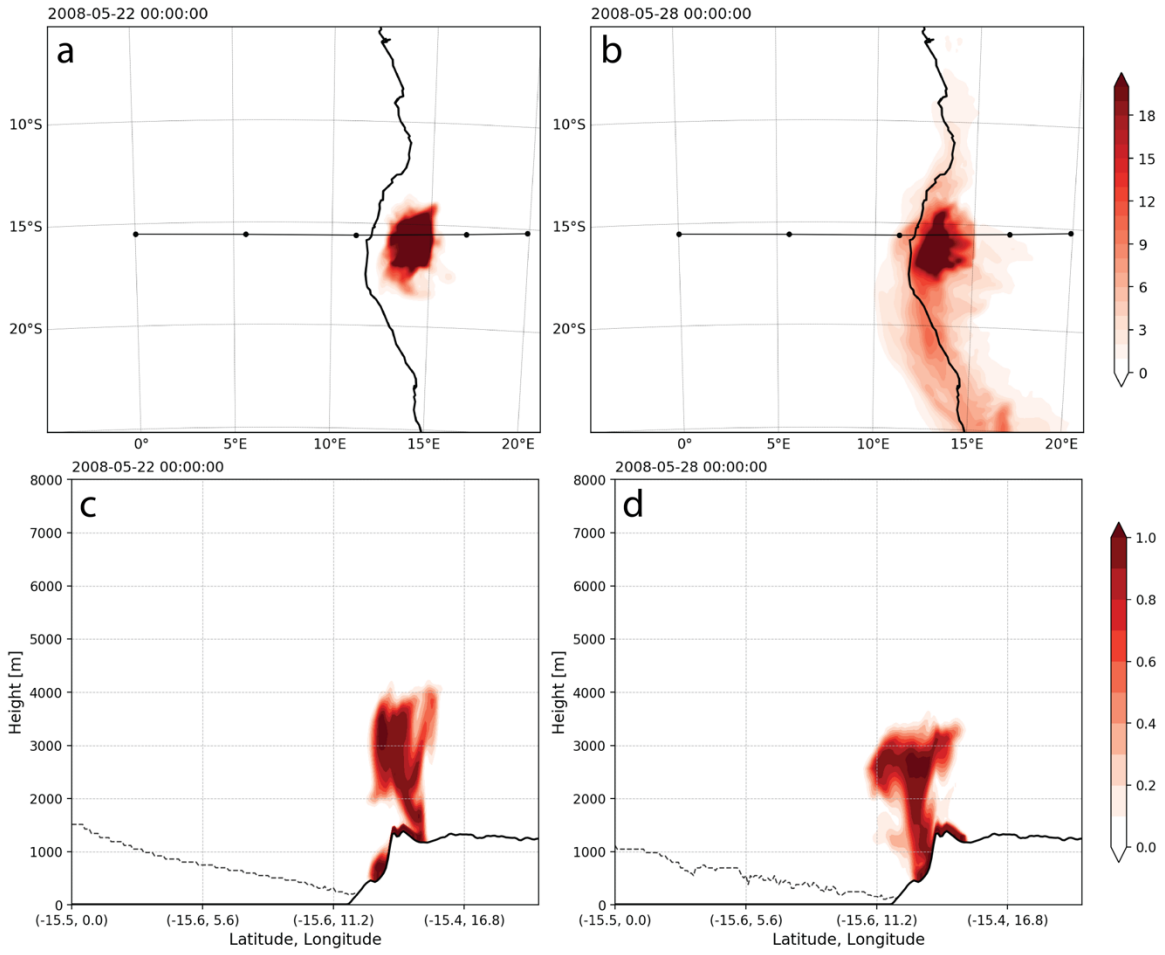


Figure 3.14. As in Fig. 3.13 but for two times during the null period (22 May 2008 0000 UTC and 28 May 2008 0000 UTC).

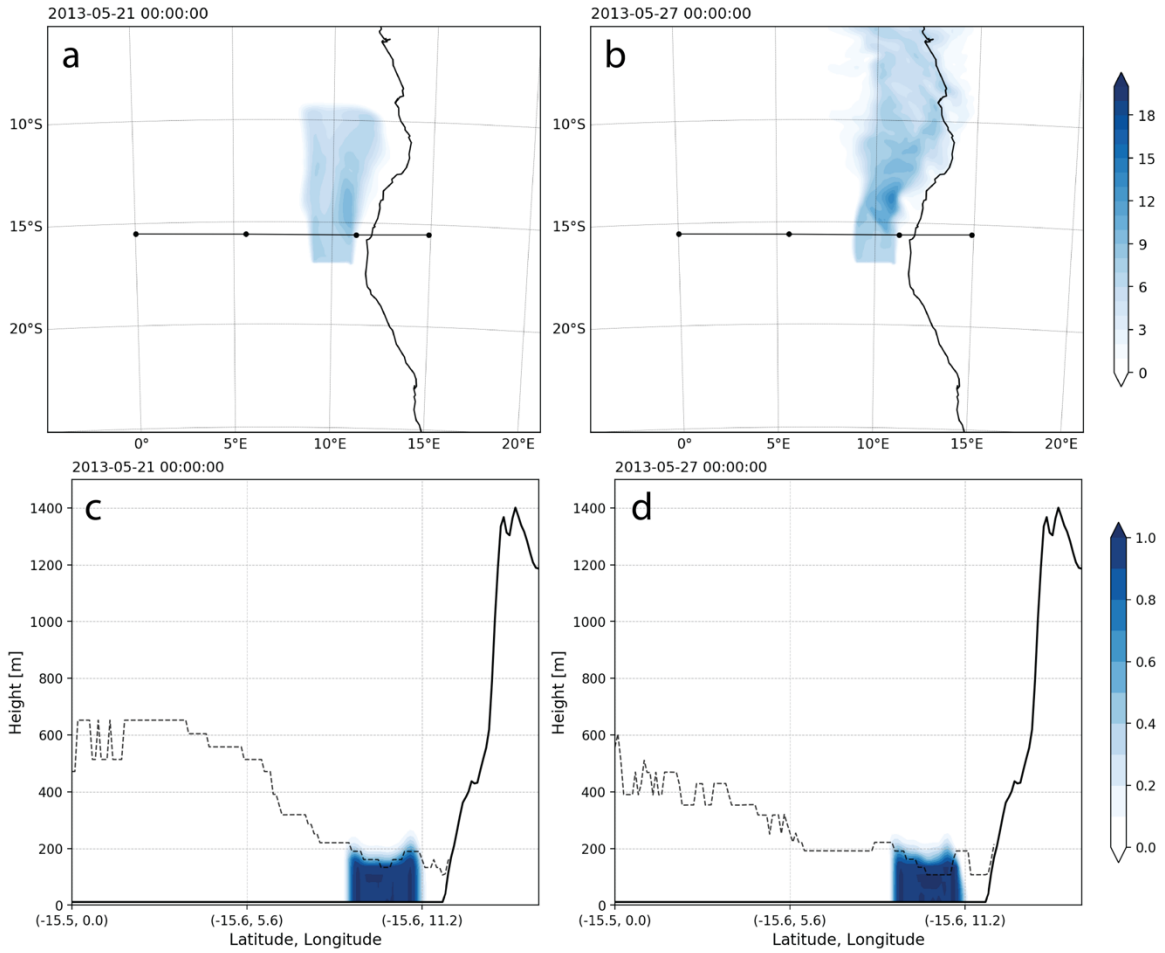


Figure 3.15. Plan views of the simulated column-integrated ‘ocean’ passive tracer field (blue shaded, dimensionless) for the same two active period times as in Fig. 3.13. (c)–(d) Vertical cross section of tracer along 15.5°S line indicated in (a) and (b) and BLH (dashed black line).

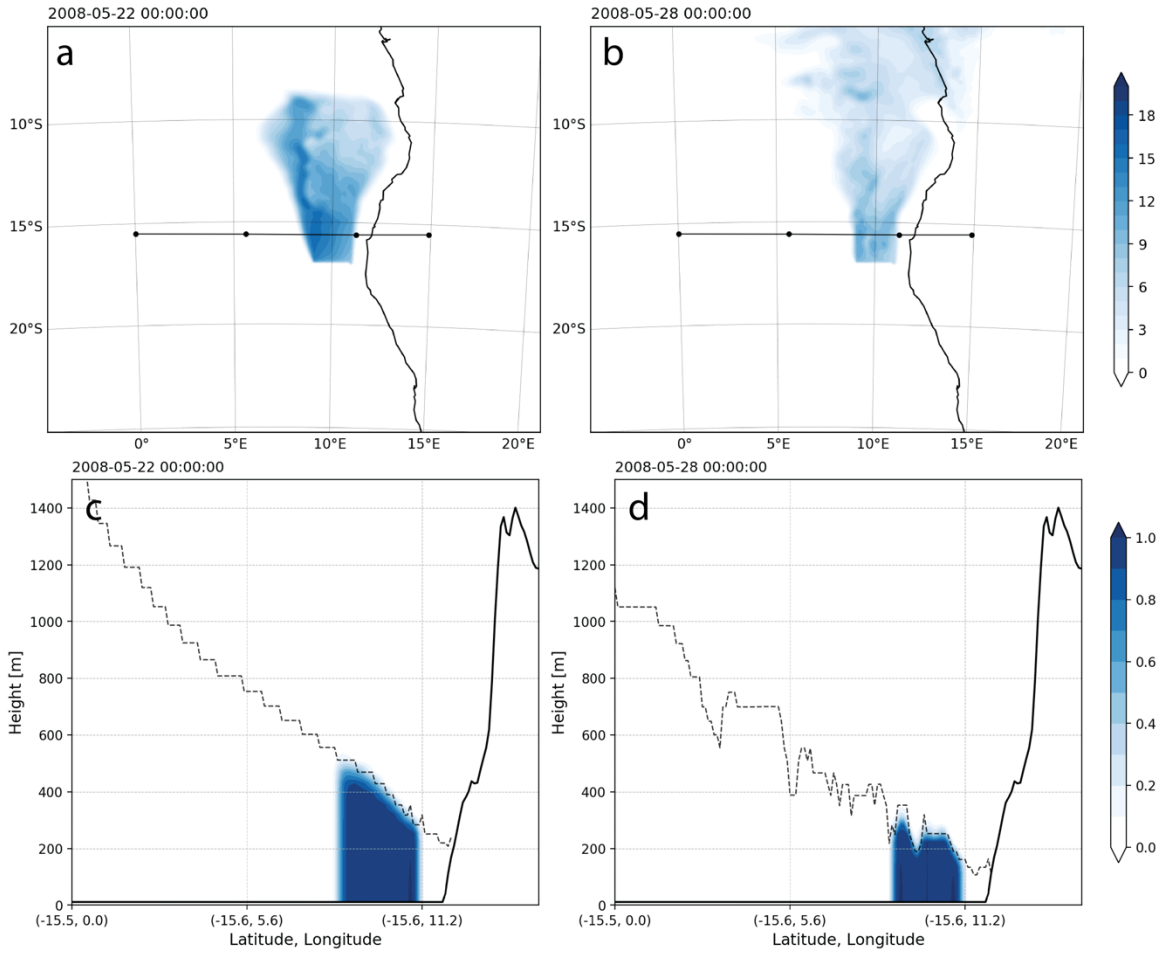


Figure 3.16. As in Fig. 3.13 but for the same two null period times as in Fig. 3.14.

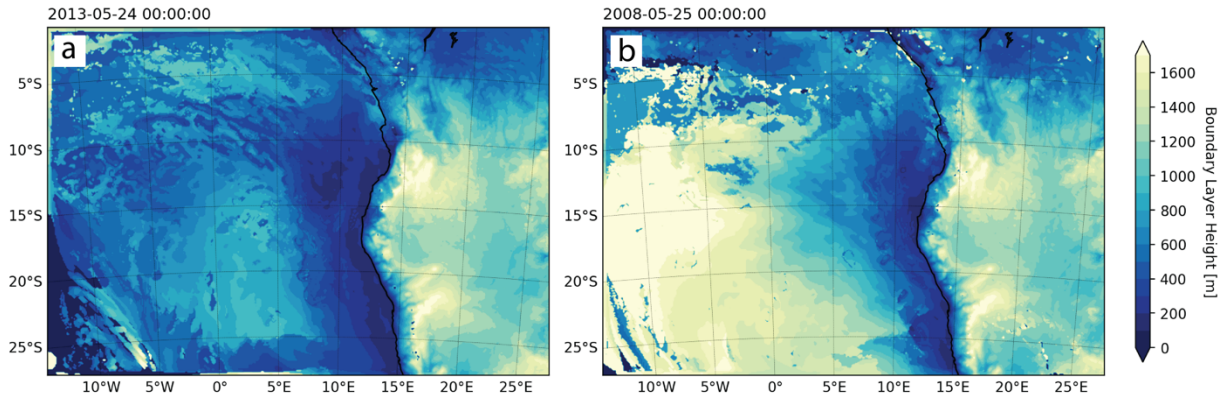


Figure 3.17. Calculated BLH (m; contoured every 100 m) for (a) active period valid 24 May 2013 0000 UTC and (b) null period valid 25 May 2008 0000 UTC.

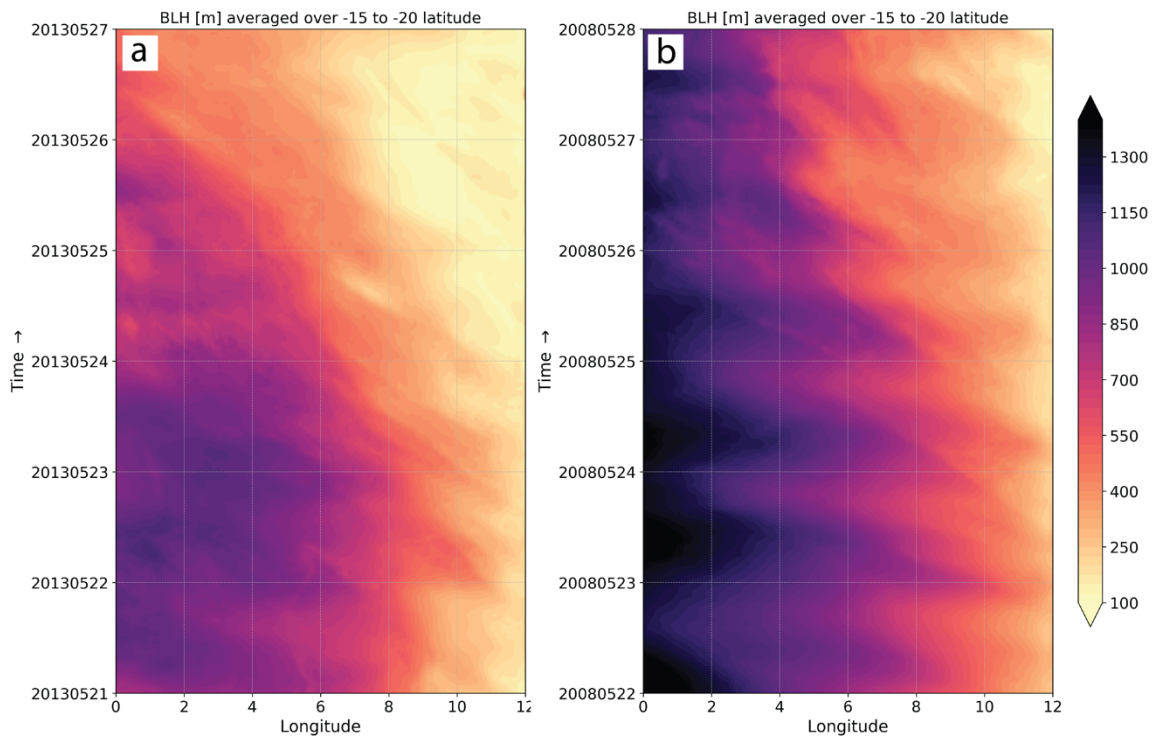


Figure 3.18. Hovmöller diagrams of BLH (m; contoured every 25 m) for the for (a) active and (b) null periods. Hovmöller diagrams are calculated over the latitude range of 15°S to 20°S (red box in Fig. 3.2a). Tick marks on y axis indicate time at 00 UTC.

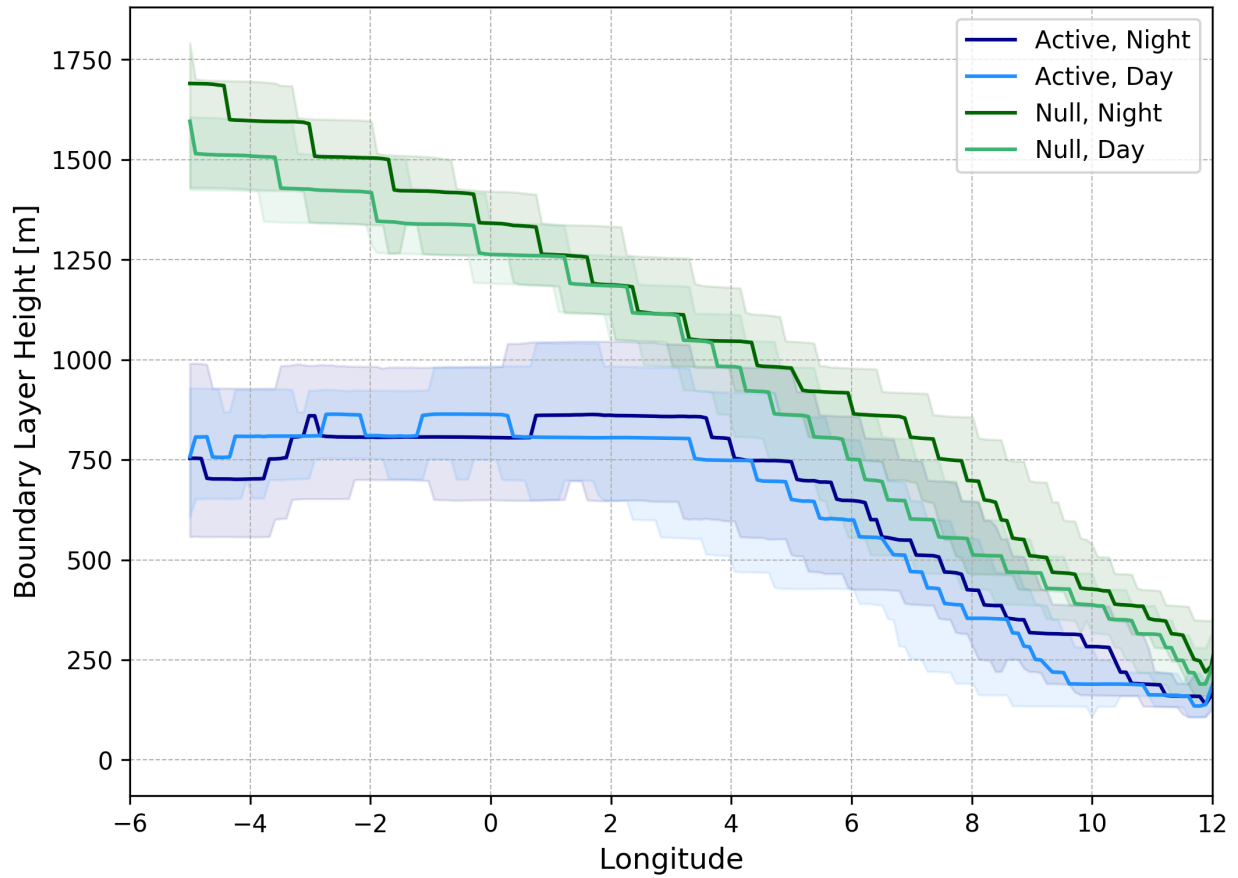


Figure 3.19. Calculated median BLH (m) as a function of longitude calculated over a latitude range from 15°S to 20°S for the null period (green) and active period (blue) during the night (0200–0600 UTC; darker colors) and during the day (1400–1800 UTC; lighter colors). Shaded regions show the interquartile range.

CHAPTER 4 Discussion

The overarching purpose of our experimental design to focus on active and null periods is to enable the identification of conditions accompanying offshore flow, which Yuter et al. (2018) proposed to be an important mechanistic component of the cloud-clearing phenomenon. Our analysis emphasizes details of the active period and differences in the active vs. the null periods, in particular, the role of the offshore flow, the importance of near-coastal low-pressure features, and boundary layer depth.

4.1 Association of offshore flow with clearing periods

We have shown that the active period is characterized by periods of strong overnight offshore flow and weak afternoon onshore flow. The opposite is true for the null period; the overnight offshore flow is weak and the afternoon onshore flow is strong. Since the active period represents a time when most of the days have cloud-clearing boundaries and the null period represents a time when most of the days do not have cloud-clearing boundaries, we speculate that the offshore and onshore flow along the coast plays a large role in determining whether or not a clearing event will happen. Our results suggest that if the flow is stronger offshore overnight, then a clearing boundary is more likely to occur compared to days when overnight offshore flow is weaker. Onshore flow would act to suppress any sort of westward flow, either advective or a propagating gravity wave, coming from the continent. This seems to be evident not only just above the boundary layer at 900 hPa but also further aloft at 700 hPa and 500 hPa.

The synoptic maps, Hovmöller diagrams, cross sections of u and w wind, and passive tracer calculations further illustrate the associations with stronger offshore flow overnight during active as compared to null periods. The Hovmöller diagrams show the patterns of offshore and onshore flow apparent in the synoptic maps. The cross sections of u and w provide additional support and

clearly show the offshore flow coupled with upward motion above the boundary layer in the active period. Finally, the passive tracer field provides additional evidence by providing a visual of the transient flow, which is not always obvious from the Hovmöller diagrams and synoptic maps, which are only at one pressure level.

Passive tracers suggest that the offshore flow from the continent during the active period can extend out as far as 0°E by the end of the simulation. This may imply that the offshore flow above the boundary layer itself could play a role in the clearing events by increasing shear-driven entrainment into the cloud as opposed to the original hypothesis that the offshore flow triggers gravity waves, after interacting with the marine boundary layer, that move out over the ocean and cause the cloud erosion.

4.2 Near-coastal low-pressure features

The prevailing low-level flow over this region is predominantly influenced by the semi-permanent, subtropical high-pressure system over the ocean. We have documented small disturbances slightly above the boundary layer (~900 hPa) which have important impacts for the offshore and onshore flow. The way these disturbances form is not clear, although our simulations suggest that they can form in multiple ways. For example, in the active period, a disturbance appears to form associated with a mid-level trough, and it then moves toward the east, likely a combination of an easterly phase speed combined with advection from the low-level flow. This is consistent with findings from de Szoeke et al. (2016), who note that mid-latitude cyclones can influence the subtropics and cause low cloud variability on multi-day timescales. A disturbance also forms in the null period; however, it does not appear to be associated with any mid-level disturbance and seems to form with the trough along the coast.

The disturbance in the null period seems to coincide with warm air columns that may have a continental origin.

The 900-hPa disturbances have important implications on the flow along the coast. In the active period, the low is positioned in such a way that it helps drive offshore flow, whereas in the null period the low seems to produce onshore flow. We recognize that the dominant high pressure which is usually present over the region in the low levels would act in such a way to promote offshore flow. Therefore, we speculate that the mean offshore flow is most representative of the “normal” conditions during this period. The null period seems to be the anomalous condition, so onshore flow associated with these disturbances represents a deviation from the norm. Because we are associating stronger overnight offshore flow with the cloud-clearing boundaries, we speculate that the cloud-clearing boundaries are the normal conditions for this region in this period and that days with strong afternoon onshore flow and weak overnight offshore flow represent anomalous days.

4.3 Impacts of Boundary layer Height

All else being equal, a deeper boundary layer is supportive of thicker stratocumulus clouds (Wood 2012). Additionally, work by Painemal and Zuidema (2010) suggests that LWP increases westward offshore in the SEP which also supports this idea as the boundary layer also deepens away from the coast. Because the active period has a shallower boundary layer than the null period, we suspect that the clouds are thinner and are more susceptible to any erosion mechanism compared to the null period. If the offshore flow triggers some sort of gravity wave, then this wave would have an easier time irreversibly eroding a thinner cloud. However, if the offshore flow increases the shear at the top of the boundary layer and increases the entrainment of warm, dry air into the cloud, then this too would erode thinner clouds more easily than thicker clouds.

We also note that models consistently underestimate boundary layer height near the coast (Wyant et al. 2015). While we do not necessarily trust the absolute height of the boundary layer in each simulation period, we have confidence in the relative boundary layer height of each simulation.

CHAPTER 5 Summary and Conclusions

In this study, we examine the physical mechanisms associated with stratocumulus cloud-clearing events over the southeast Atlantic. We use the WRF model to run simulations over days where there are several days of cloud clearings (an active period) and simulations over days where there are several days without clouds clearings (a null period). We focus on analyzing the overnight offshore flow with synoptic maps, Hovmöller diagrams, cross sections, and passive tracer fields. We document different conditions associated with each period to understand its role in cloud-clearing boundaries. Our main conclusions are as follows:

- “Active” periods with cloud-clearing events have stronger overnight offshore flow than “null” periods without clearing events. We suspect that the offshore flow plays an important role on periods with clearing events by either interacting with the boundary layer to cause gravity waves which clear the cloud or by increasing the shear at the top of the boundary layer which would increase dry air entrainment into the cloud.
- The dominant overnight offshore and afternoon onshore flows that delineate active from null periods are associated with synoptic scale disturbances and not explained by temperature differences over land.
- The overnight offshore flow is warmer than the boundary layer and therefore overruns the boundary layer. We speculate that the interaction of the offshore flow with the top of the inversion has important implications for entrainment processes that lead to cloud dissipation.
- Active periods have lower boundary layer heights than null periods. All else being equal, lower boundary layer heights are associated with thinner clouds, which may cause the clouds in the active period to be more susceptible to erosion.

The WRF simulations suggest an additional cloud-clearing hypothesis to investigate; the offshore flow increases the shear at the top of the boundary layer and enhances entrainment of warm, dry air into the cloud, which leads to rapid erosion. The work here does not explain any sort of interaction the offshore flow might have with the boundary layer itself, which may trigger gravity waves.

One major difficulty in this work is the separation of temporal and spatial scales between the synoptic and diurnal. The assumption of a diurnal cycle superimposed over a quasi-steady, barotropic background is plainly an oversimplification. The background synoptic state is highly varying on multi-day timescales, as demonstrated by de Szoeke et al. (2016). This reality makes teasing the two scales apart — and unambiguously identifying the conditions conducive to cloud-clearing events — highly difficult. As part of disentangling the synoptic and diurnal contributions to the variability, an additional analysis should be done to examine the role of the ageostrophic flow during these periods. Specifically, a more thorough momentum budget analysis should be completed to better separate the different mechanisms presented in this work.

Some of the work presented here indicates that the shape and convexity of the coastline in this region also likely play a role in these boundaries and the flow of the region. Further analysis should be completed to examine the implications of the coastline and the resulting localized convergence and divergence in determining days with or without clearing events. Additional simulations removing or reducing the topography would help in studying the effects of the terrain on the cloud-clearing boundaries.

The work presented here only analyzes simulations during the month of May; however, our understanding of these events could also be improved by simulations which cover different months or seasons. Particularly, simulations in the month of January, when the frequency of

cloud-clearing boundaries is at a minimum (Yuter et al. 2018), would help understand the large-scale synoptic differences during these seasons.

While the results of this study are helpful, using mesoscale models and the limited observations that are available can only aid so much in our understanding of these events. Ideally, aircraft data including dropsondes, lidar data, and cloud radar data transecting through a clearing boundary would advance our overall knowledge of the cloud-clearing boundaries in this region and help to address some of the uncertainties discussed here.

APPENDICES

Appendix A

To test the sensitivity of the boundary layer parameterizations, we compared the initial simulation using Mellor–Yamada–Janjic (MYJ) scheme with the Yonsei University scheme and the Mellor–Yamada Nakanishi Niino (MYNN) Level–2.5 scheme (Hong et al. 2006; Janjic 1994; Nakanishi and Niino 2006).

We analyzed the diurnal cycle over the land in the three simulations to see how they compared. We averaged the 2-m and skin (land surface) temperatures over the black box in Fig. A1 for each output time for each of the simulations. Results are shown in Fig. A2. The different parameterizations showed modest differences. The Yonsei scheme seems to have a higher daily maximum skin temperature than the other schemes (Fig. A2c). The MYNN scheme seems to have a lower skin and 2m minimum temperature than the other two schemes (Fig. A2b). The average minimum temperature for each scheme is shown in Table 2. However, the modest differences across the parameterizations do not appear to lead to large differences in simulation results and do not impact our research conclusions.

Boundary layer Scheme	Average Minimum Temperature (K)
Mellor–Yamada–Janjic (MYJ)	286.1
Yonsei University	285.9
Mellor–Yamada Nakanishi Niino (MYNN)	283.9

Table A1. Average minimum temperature for different Boundary layer schemes.

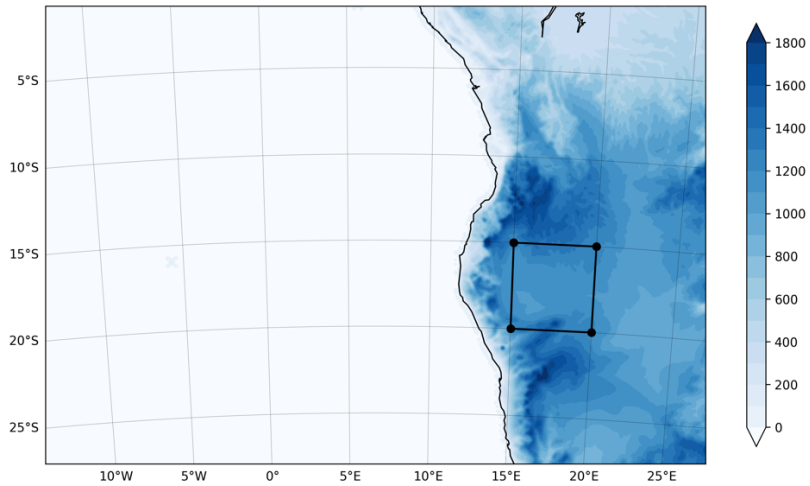


Figure A1. Map of Africa showing temperature analysis region in black box.

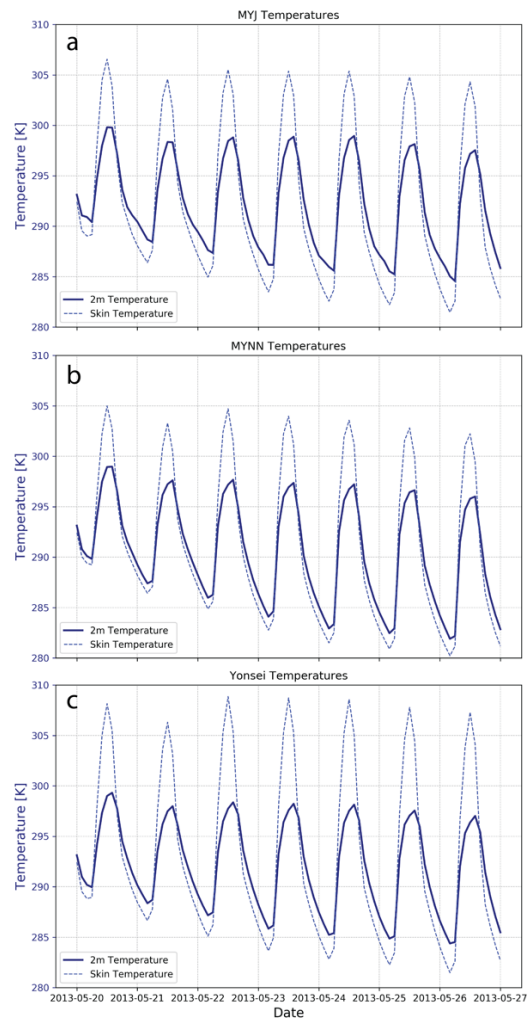


Figure A2. Diurnal cycle of temperature for (a) MYJ, (b) MYNN, and (c) Yonsei simulations. Temperatures averaged over box in Fig. A1.

Appendix B

This section contains descriptions and captions for each animation referenced above. Animations can be accessed through this link: <https://bit.ly/2LJ6OS3>

Animation 3.1: Simulated 900-hPa heights (m; contoured every 10 m) and wind valid every hour from 20 May 2013 0000 UTC through 27 May 2013 0000 UTC from the active period.

Animation 3.2: As in Animation 3.1 but valid every hour from 21 May 2008 0000 UTC through 28 May 2008 0000 UTC from the null period.

Animation 3.3: Cross section along 15°S of w (shaded; contoured every 1 cm s⁻¹), u (grey lines, contoured every 1 m s⁻¹, dashed indicates negative values) and BLH (bold black line) valid every hour from 20 May 2013 0000 UTC through 27 May 2013 0000 UTC from the active period.

Animation 3.4: As in Animation 3.3 but valid every hour from 21 May 2008 0000 UTC through 28 May 2008 0000 UTC from the null period.

Animation 3.5: Plan views of the simulated column-integrated ‘land’ passive tracer field (red shaded, dimensionless) valid every hour from 20 May 2013 0000 UTC through 27 May 2013 0000 UTC from the active period.

Animation 3.6: Vertical cross section of ‘land’ passive tracer field (red shaded, dimensionless) along 15.5°S line indicated in Fig. 3.13a,b and BLH (dashed black line) valid every hour from 20 May 2013 0000 UTC through 27 May 2013 0000 UTC from the active period.

Animation 3.7: As in Animation 3.5 but valid every hour from 21 May 2008 0000 UTC through 28 May 2008 0000 UTC from the null period.

Animation 3.8: As in Animation 3.6 but valid every hour from 21 May 2008 0000 UTC through 28 May 2008 0000 UTC from the null period.

Animation 3.9: Plan views of the simulated column-integrated ‘ocean’ passive tracer field (blue shaded, dimensionless) valid every hour from 20 May 2013 0000 UTC through 27 May 2013 0000 UTC for the active period.

Animation 3.10: Vertical cross section of ‘ocean’ passive tracer field (blue shaded, dimensionless) along 15.5°S line indicated in Fig. 3.13a,b and BLH (dashed black line) valid every hour from 20 May 2013 0000 UTC through 27 May 2013 0000 UTC for the active period.

Animation 3.11: As in Animation 3.9 but valid every hour from 21 May 2008 0000 UTC through 28 May 2008 0000 UTC from the null period.

Animation 3.12: As in Animation 3.10 but valid every hour from 21 May 2008 0000 UTC through 28 May 2008 0000 UTC from the null period.

Appendix C

In order to see if differences in overnight cooling were associated with increased downward motion in the active period, we did a similar temperature analysis described in Appendix A. We averaged 2-m temperatures over the box defined in Fig. C1 for both the active and the null period. If the overnight cooling were to be associated with more downward motion in the active period, we would expect the overnight temperatures to be cooler than in the null period. Figure C1 shows that the diurnal temperatures over the land are of similar magnitude for each period. If anything, the null period may have a slightly lower average of minimum temperature since there are a couple of days where the minimum temperature in the active period appears to be warmer than average. This provides support for our hypothesis that the increased downward motion over land in the active period (fig. 3.3c) is associated with the increased offshore flow overnight and is not due to stronger cooling over land.

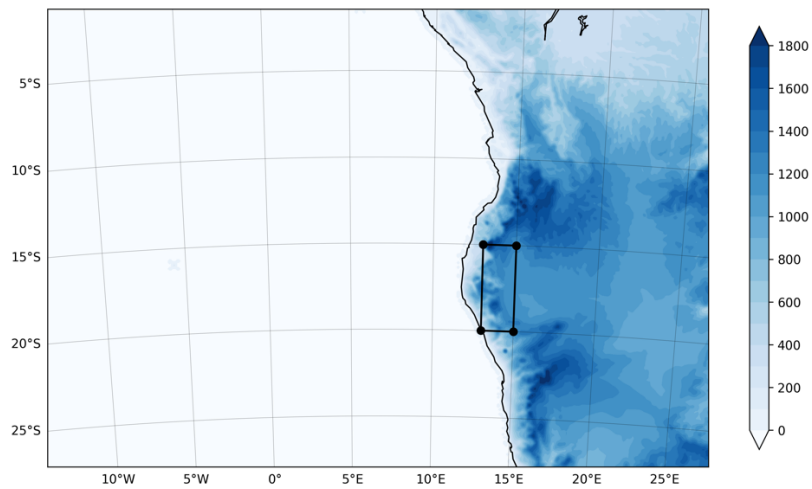


Figure C1. Map of Africa showing temperature analysis region in the black box.

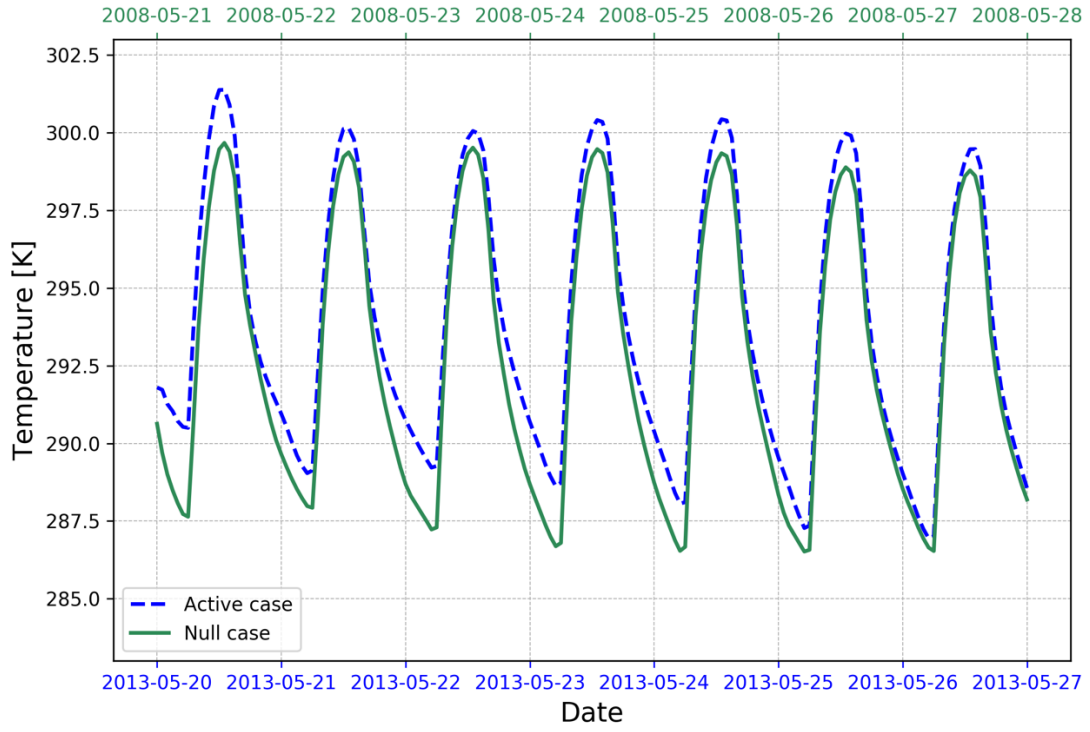


Figure C2. Diurnal cycle for active period (blue, dashed line) and null period (green, solid line) for the region in Figure C1.

Appendix D

Figure D1 shows the geostrophic and ageostrophic wind components for the active period. 950-hPa geostrophic u and ageostrophic u are shown in panels a and b, respectively. 800-hPa geostrophic u and ageostrophic u are shown in panels c and d, respectively. Figure D2 shows the same but for the null period. The main purpose here is to show that the striped features shown in the 900-hPa ageostrophic u wind in Figs. 3.5b and 3.6b are present both below at 950 hPa and above at 800 hPa. The stripes are particularly prominent at 900 hPa in the null period (Fig. 3.6b) and are also clear here at 950 hPa and 800 hPa (Fig. D1b,d). This striped pattern suggested that the diurnal onshore and offshore turning of the coastal jet extends over 10° longitude offshore (~ 1000 km). The response of the jet this far offshore is not well understood. More work, potentially with satellite derived winds, should be done to examine this feature.

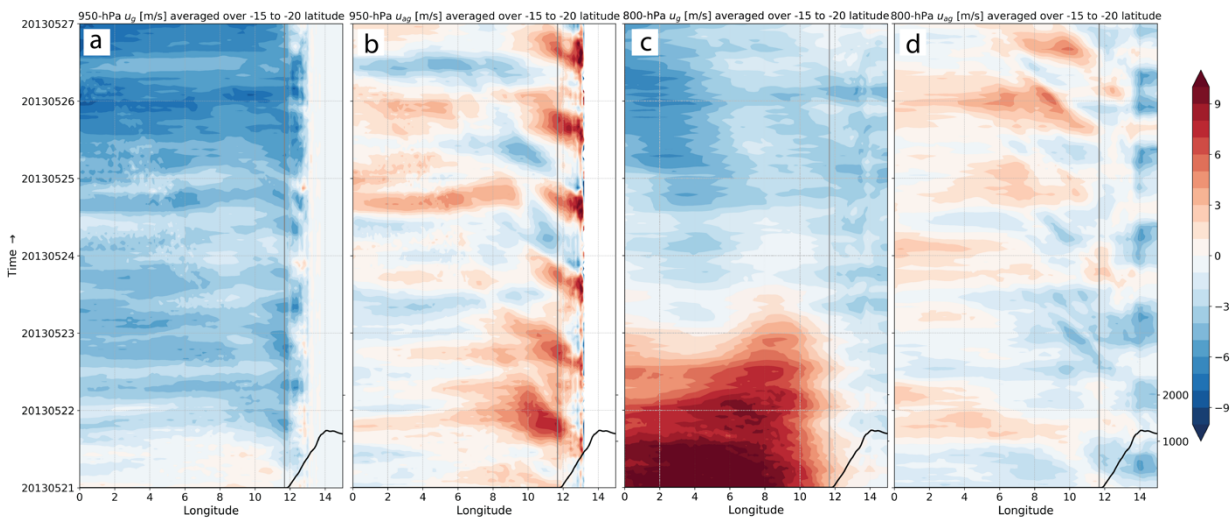


Figure D1. Hovmöller diagrams of the geostrophic and ageostrophic components of the 950-hPa and 800-hPa horizontal wind for the active period. (a) 950-hPa u_g , (b) 950-hPa u_a , (c) 800-hPa u_g , and (d) 800-hPa u_a (m s^{-1} ; contoured every 1 m s^{-1}). As in Figs. 3.3 and 3.4, Hovmöller diagrams are calculated over the latitude range of 15°S to 20°S (red box in Fig. 3.2a). The black line in the bottom corner indicates the average coastline over this region and the bold grey line shows where the average coastline begins. Tick marks on y axis indicate time at 00 UTC.

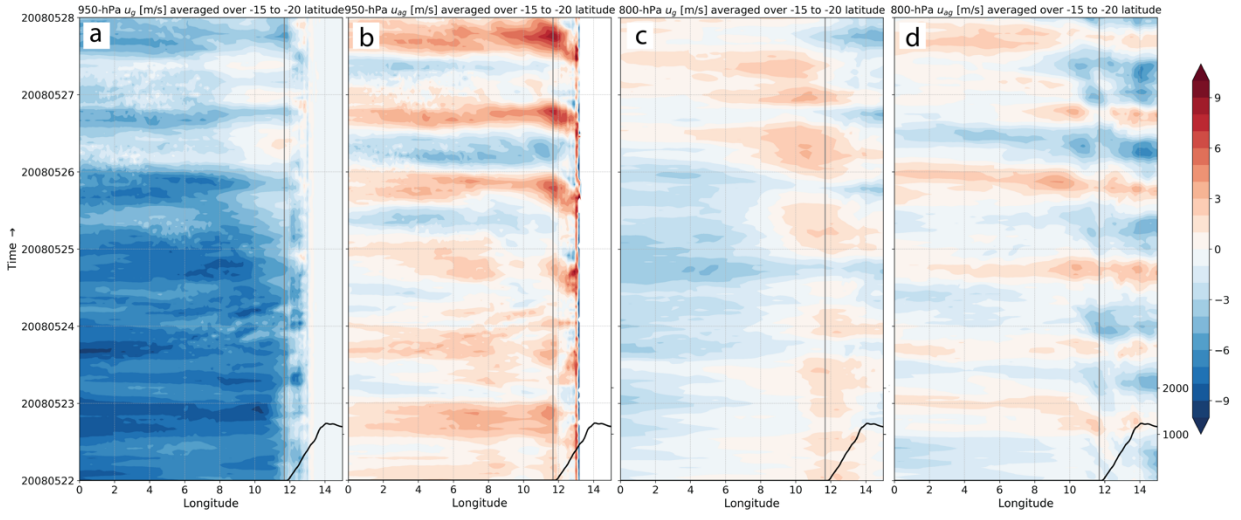


Figure D2. As in Fig. D1 but for null period.

REFERENCES

- Allen, G., G. Vaughan, T. Toniazzo, H. Coe, P. Connolly, S. E. Yuter, C. D. Burleyson, P. Minnis, and J. K. Ayers, 2013: Gravity-wave-induced perturbations in marine stratocumulus. *Q J Roy Meteor Soc*, **139**, 32-45.
- Birch, C. E., and M. J. Reeder, 2013: Wave-cloud lines over northwest Australia. *Q J Roy Meteor Soc*, **139**, 1311-1326.
- Blaylock, B. K., J. D. Horel, and E. T. Crosman, 2017: Impact of Lake Breezes on Summer Ozone Concentrations in the Salt Lake Valley. *J Appl Meteorol Clim*, **56**, 353-370.
- Bony, S., and J. L. Dufresne, 2005: Marine boundary layer clouds at the heart of tropical cloud feedback uncertainties in climate models. *Geophys Res Lett*, **32**.
- Burleyson, C. D., and S. E. Yuter, 2015: Subdiurnal Stratocumulus Cloud Fraction Variability and Sensitivity to Precipitation. *J Climate*, **28**, 2968-2985.
- Clarke, R., 1972: The morning glory: An atmospheric hydraulic jump. *Journal of Applied Meteorology*, **11**, 304-311.
- Connolly, P. J., G. Vaughan, P. Cook, G. Allen, H. Coe, T. W. Choularton, C. Dearden, and A. Hill, 2013: Modelling the effects of gravity waves on stratocumulus clouds observed during VOCALS-UK. *Atmos Chem Phys*, **13**, 7133-7152.
- Crosbie, E., Z. Wang, A. Sorooshian, P. Y. Chuang, J. S. Craven, M. M. Coggon, M. Brunke, X. B. Zeng, H. Jonsson, R. K. Woods, R. C. Flagan, and J. H. Seinfeld, 2016: Stratocumulus Cloud Clearings and Notable Thermodynamic and Aerosol Contrasts across the Clear-Cloudy Interface. *J Atmos Sci*, **73**, 1083-1099.
- de Szoek, S. P., K. L. Verlinden, S. E. Yuter, and D. B. Mechem, 2016: The Time Scales of Variability of Marine Low Clouds. *J Climate*, **29**, 6463-6481.
- Dee, D. P., S. M. Uppala, A. J. Simmons, P. Berrisford, P. Poli, S. Kobayashi, U. Andrae, M. A. Balsameda, G. Balsamo, P. Bauer, P. Bechtold, A. C. M. Beljaars, L. van de Berg, J. Bidlot, N. Bormann, C. Delsol, R. Dragani, M. Fuentes, A. J. Geer, L. Haimberger, S. B. Healy, H. Hersbach, E. V. Holm, L. Isaksen, P. Kallberg, M. Kohler, M. Matricardi, A. P. McNally, B. M. Monge-Sanz, J. J. Morcrette, B. K. Park, C. Peubey, P. de Rosnay, C. Tavolato, J. N. Thepaut, and F. Vitart, 2011: The ERA-Interim reanalysis: configuration and performance of the data assimilation system. *Q J Roy Meteor Soc*, **137**, 553-597.
- Dudhia, J., 1989: Numerical Study of Convection Observed during the Winter Monsoon Experiment Using a Mesoscale Two-Dimensional Model. *J Atmos Sci*, **46**, 3077-3107.
- Garreaud, R. D., and J. Rutllant, 2003: Coastal lows along the subtropical west coast of South America: Numerical simulation of a typical case. *Mon Weather Rev*, **131**, 891-908.
- Garreaud, R. D., and R. Muñoz, 2004: The diurnal cycle in circulation and cloudiness over the subtropical southeast Pacific: A modeling study. *J Climate*, **17**, 1699-1710.

- Garreaud, R. D., and R. C. Muñoz, 2005: The low-level jet off the west coast of subtropical South America: Structure and variability. *Mon Weather Rev*, **133**, 2246-2261.
- Garreaud, R. D., J. A. Rutllant, and H. Fuenzalida, 2002: Coastal lows along the subtropical west coast of South America: Mean structure and evolution. *Mon Weather Rev*, **130**, 75-88.
- Gelaro, R., W. McCarty, M. J. Suarez, R. Todling, A. Molod, L. Takacs, C. A. Randles, A. Darmenov, M. G. Bosilovich, R. Reichle, K. Wargan, L. Coy, R. Cullather, C. Draper, S. Akella, V. Buchard, A. Conaty, A. M. da Silva, W. Gu, G. K. Kim, R. Koster, R. Lucchesi, D. Merkova, J. E. Nielsen, G. Partyka, S. Pawson, W. Putman, M. Rienecker, S. D. Schubert, M. Sienkiewicz, and B. Zhao, 2017: The Modern-Era Retrospective Analysis for Research and Applications, Version 2 (MERRA-2). *J Climate*, **30**, 5419-5454.
- George, R. C., and R. Wood, 2010: Subseasonal variability of low cloud radiative properties over the southeast Pacific Ocean. *Atmos Chem Phys*, **10**, 4047-4063.
- Hartmann, D. L., M. E. Ockertbell, and M. L. Michelsen, 1992: The Effect of Cloud Type on Earths Energy-Balance - Global Analysis. *J Climate*, **5**, 1281-1304.
- Hersbach, H., and D. Dee, 2016: ERA-5 reanalysis is in production. *ECMWF newsletter*, **7**.
- Holton, J. R., 2004: *An Introduction to Dynamic Meteorology*. 4 ed. Vol. 88, Academic Press.
- Hong, S. Y., Y. Noh, and J. Dudhia, 2006: A new vertical diffusion package with an explicit treatment of entrainment processes. *Mon Weather Rev*, **134**, 2318-2341.
- Janjic, Z. I., 1994: The Step-Mountain Eta Coordinate Model - Further Developments of the Convection, Viscous Sublayer, and Turbulence Closure Schemes. *Mon Weather Rev*, **122**, 927-945.
- Kain, J. S., 2004: The Kain-Fritsch convective parameterization: An update. *J Appl Meteorol*, **43**, 170-181.
- Klein, S. A., and D. L. Hartmann, 1993: The Seasonal Cycle of Low Stratiform Clouds. *J Climate*, **6**, 1587-1606.
- Kloesel, K. A., 1992: Marine Stratocumulus Cloud Clearing Episodes Observed during Fire. *Mon Weather Rev*, **120**, 565-578.
- Mlawer, E. J., S. J. Taubman, P. D. Brown, M. J. Iacono, and S. A. Clough, 1997: Radiative transfer for inhomogeneous atmospheres: RRTM, a validated correlated-k model for the longwave. *J Geophys Res-Atmos*, **102**, 16663-16682.
- Montecinos, A., R. C. Muñoz, S. Oviedo, A. Martinez, and V. Villagran, 2017: Climatological Characterization of Puelche Winds down the Western Slope of the Extratropical Andes Mountains Using the NCEP Climate Forecast System Reanalysis. *J Appl Meteorol Clim*, **56**, 677-696.

Morrison, H., G. Thompson, and V. Tatarskii, 2009: Impact of Cloud Microphysics on the Development of Trailing Stratiform Precipitation in a Simulated Squall Line: Comparison of One- and Two-Moment Schemes. *Mon Weather Rev*, **137**, 991-1007.

Nakanishi, M., and H. Niino, 2006: An improved Mellor-Yamada level-3 model: Its numerical stability and application to a regional prediction of advection fog. *Bound-Lay Meteorol*, **119**, 397-407.

Nelson, K. J., D. B. Mechem, and Y. L. Kogan, 2016: Evaluation of Warm-Rain Microphysical Parameterizations in Mesoscale Simulations of the Cloudy Marine Boundary Layer. *Mon Weather Rev*, **144**, 2137-2154.

O'Dell, C. W., F. J. Wentz, and R. Bennartz, 2008: Cloud liquid water path from satellite-based passive microwave observations: A new climatology over the global oceans. *J Climate*, **21**, 1721-1739.

Painemal, D., and P. Zuidema, 2010: Microphysical variability in southeast Pacific Stratocumulus clouds: synoptic conditions and radiative response. *Atmos Chem Phys*, **10**, 6255-6269.

Parish, T. R., 2000: Forcing of the summertime low-level jet along the California coast. *J Appl Meteorol*, **39**, 2421-2433.

Rahn, D. A., and R. Garreaud, 2010: Marine boundary layer over the subtropical southeast Pacific during VOCALS-REx - Part 1: Mean structure and diurnal cycle. *Atmos Chem Phys*, **10**, 4491-4506.

Rahn, D. A., and R. D. Garreaud, 2014: A synoptic climatology of the near-surface wind along the west coast of South America. *Int J Climatol*, **34**, 780-792.

Rutllant, J., and V. Montecino, 2002: Multiscale upwelling forcing cycles and biological response off north-central Chile. *Rev Chil Hist Nat*, **75**, 217-231.

Rutllant, J. A., and R. D. Garreaud, 2004: Episodes of strong flow down the western slope of the subtropical Andes. *Mon Weather Rev*, **132**, 611-622.

Skamarock, W. C., J. B. Klemp, J. Dudhia, D. O. Gill, D. M. Barker, M. G. Duda, X.-Y. Huang, W. Wang, and J. G. Powers, 2008: A Description of the Advanced Research WRF Version 3. *NCAR Tech. Note NCAR/TN-475+STR*, 113.

Smagorinsky, J., 1963: General circulation experiments with the primitive equations: I. The basic experiment. *Mon Weather Rev*, **91**, 99-164.

Stevens, B., G. Vali, K. Comstock, R. Wood, M. C. van Zanten, P. H. Austin, C. S. Bretherton, and D. H. Lenschow, 2005: Pockets of open cells and drizzle in marine stratocumulus. *B Am Meteorol Soc*, **86**, 51-57.

Tewari, M., F. Chen, W. Wang, J. Dudhia, M. A. LeMone, K. Mitchell, M. Ek, G. Gayno, J. Wegiel, and R. H. Cuenca, 2004: Implementation and verification of the unified NOAA land surface model in the WRF model. *20th conference on weather analysis and forecasting/16th conference on numerical weather prediction*, 11-15.

Wood, R., 2012: Stratocumulus Clouds. *Mon Weather Rev*, **140**, 2373-2423.

Wyant, M. C., C. S. Bretherton, R. Wood, G. R. Carmichael, A. Clarke, J. Fast, R. George, W. I. Gustafson, C. Hannay, A. Lauer, Y. Lin, J. J. Morcrette, J. Mulcahy, P. E. Saide, S. N. Spak, and Q. Yang, 2015: Global and regional modeling of clouds and aerosols in the marine boundary layer during VOCALS: the VOCA intercomparison. *Atmos Chem Phys*, **15**, 153-172.

Yuter, S. E., J. D. Hader, M. A. Miller, and D. B. Mechem, 2018: Abrupt cloud clearing of marine stratocumulus in the subtropical southeast Atlantic. *Science*.

Zuidema, P., P. Chang, B. Medeiros, B. P. Kirtman, R. Mechoso, E. K. Schneider, T. Toniazzo, I. Richter, R. J. Small, K. Bellomo, P. Brandt, S. de Szoeke, J. T. Farrar, E. Jung, S. Kato, M. K. Li, C. Patricola, Z. Y. Wang, R. Wood, and Z. Xu, 2016: Challenges and Prospects for Reducing Coupled Climate Model SST Biases in the Eastern Tropical Atlantic and Pacific Oceans: The U.S. CLIVAR Eastern Tropical Oceans Synthesis Working Group. *B Am Meteorol Soc*, **97**, 2305-+.